Shell-model study on spectroscopic properties in the region "south" of ^{208}Pb

Cenxi Yuan [1,*], Menglan Liu [1], Noritaka Shimizu [2], Zs. Podolyák [3], Toshio Suzuki [4,5]
Takaharu Otsuka [6,7,8,9] and Zhong Liu [10,11]

[1]*Sino-French Institute of Nuclear Engineering and Technology, Sun Yat-Sen University, Zhuhai, Guangdong 519082, China*
[2]*Center for Nuclear Study, University of Tokyo, Hongo, Bunkyo-ku, Tokyo 113-0033, Japan*
[3]*Department of Physics, University of Surrey, Guildford, Surrey GU2 7XH, United Kingdom*
[4]*Department of Physics, College of Humanities and Sciences, Nihon University, Sakurajosui 3, Setagaya-ku, Tokyo 156-8550, Japan*
[5]*National Astronomical Observatory of Japan, Mitaka, Tokyo 181-8588, Japan*
[6]*Department of Physics, University of Tokyo, Hongo, Bunkyo-ku, Tokyo 113-0033, Japan*
[7]*RIKEN Nishina Center, 2-1 Hirosawa, Wako, Saitama 351-0198, Japan*
[8]*National Superconducting Cyclotron Laboratory, Michigan State University, East Lansing, Michigan 48824, USA*
[9]*Instituut voor Kern-en Stralingsfysica, Katholieke Universiteit Leuven, B-3001 Leuven, Belgium*
[10]*Institute of Modern Physics, Chinese Academy of Sciences, Lanzhou 730000, China*
[11]*School of Nuclear Science and Technology, University of Chinese Academy of Sciences, Beijing 100049, China*

Background: The properties of nuclei located in the region "south" of ^{208}Pb are important for understanding the r-process nucleosynthesis. While some isomeric states and their spectroscopic properties have been investigated experimentally in neutron-rich Pb, Tl, and Hg isotopes recently, a large portion of the area still remains unreachable.

Purpose: We aim to study the properties of nuclei in the region south of ^{208}Pb, including the binding and excitation energies and electromagnetic properties, in order to predict unknown properties of these nuclei, such as isomerism, utilizing a theoretical model which describes the experimentally known properties precisely. We also address whether the $N = 126$ shell closure is robust or not when the proton number decreases from ^{208}Pb.

Methods: We performed large-scale shell-model calculations with a new Hamiltonian suggested in the present work. The model space is taken as the 5 proton orbits within $50 < Z \leqslant 82$ and the 13 neutron orbits within $82 < N \leqslant 184$, and one-particle-one-hole excitation is allowed across the $N = 126$ gap. The Hamiltonian is constructed by combining the existing Hamiltonians, KHHE (with adjustment of its proton-proton part) and KHPE, and the monopole-based universal interaction.

Results: The shell-model results well reproduce the experimentally observed binding energies and spectroscopic properties, such as isomerism, core excitation, and electromagnetic properties. Some possible isomeric states in neutron-rich Pb, Tl, and Hg isotopes are predicted with transition energies and half-lives. The $N = 126$ shell gap is predicted to be robust from $Z = 82$ down to 72 with minor reduction. We also examine the effective charges and the quenching of the g factors suitable for this region by comparisons between observed and calculated electromagnetic properties.

Conclusions: A new Hamiltonian is constructed for nuclei in the region south of ^{208}Pb, mainly including Pb, Tl, Hg, Au, Pt, Ir, Os, Re, and W isotopes around $N = 126$, and provides them reasonable descriptions on nuclear properties including binding energies, excitation energies, and electromagnetic properties through shell-model studies. The present Hamiltonian and discussions provide fruitful information for future measurements and theoretical investigations for nuclei in this region, especially those around the $N = 126$ shell, including the recommended effective charges and g factors, the predicted binding energies, isomeric states, and core-excited states.

I. INTRODUCTION

The rapid neutron-capture process (r process) is believed to be a key origin of the heavy nuclides found in nature [1]. The properties of nuclei, such as masses, half-lives, and neutron-capture cross sections, are essential for understanding the r-process nucleosynthesis [2]. For example, the $A = 195$ abundance peak in the r process is associated with the properties of nuclei around $N = 126$ [1]. However, the measurements of many important nuclear data are beyond the present experimental access. Theoretical predictions of the unknown data of $N = 126$ isotones below ^{208}Pb and nearby nuclei are of crucial significance.

*yuancx@mail.sysu.edu.cn

Some isomers have been discovered in the region around ^{208}Pb [3], but many more are expected from shell-model calculations. On the neutron-rich side of the stability line in this region, the 8_1^+ seniority isomers have been observed up to ^{216}Pb and ^{210}Hg in their respective isotopic chains [4,5]. The KISS (KEK Isotope Separation System) project aims to measure the properties of the ground and isomeric states in the region "south" of ^{208}Pb [6,7], such as the magnetic moments of the ground and isomeric states of ^{199}Pt [8]. Reliable descriptions of the known levels and electromagnetic transition rates are necessary for a model to make new predictions in this region. The β-decay properties of long-lived isomers in this region could also be relevant to network calculations in the r-process nucleosynthesis.

Also, the stability of $N = 126$ shell closure in the neutron-rich side attracts much interest. In nuclei with extreme proton-neutron ratio, traditional proton (neutron) magic numbers may disappear and new ones may emerge, manifesting dynamic shell evolution with isospin. Recent investigations revealed a significant sd component in both the ground and excited states in ^{12}Be [9,10], indicating the disappearance of the $N = 8$ shell closure in very neutron-rich Be isotopes. The $N = 20$ shell closure vanishes below ^{34}Si, the northern boundary of the "island of inversion" [11]. In medium mass nuclei, the $Z = 40$ subshell in neutron-rich Ag isotopes with neutron numbers approaching $N = 82$ is found to be very fragile [12].

So far, experimental information is scarce on the size of the $N = 126$ shell gap in the most neutron-rich isotopes with $Z \leqslant 82$. An observation of the excited states in ^{204}Pt supported an unquenched $N = 126$ gap [13]. Some neutron core-excited states are found at excitation energies larger than 2 MeV in ^{208,209}Pb, ^{207}Tl, and ^{206}Hg [14,15]. At present, it is still challenging to observe neutron core-excited states in $N = 126$ isotones below ^{206}Hg. It is necessary to construct a theoretical model, which describes the experimentally available data of ^{207}Tl and ^{206}Hg precisely, for a reliable prediction of the evolution of the $N = 126$ shell gap with decreasing atomic number Z.

The nuclear shell model is one of the best models to describe the above structure properties in a unified way, including binding energies, levels, shell gaps, electromagnetic transition rates, isomers, and β decays. The present work aims to provide a shell-model investigation based on a newly constructed Hamiltonian for the description of spectroscopic properties in the region around ^{208}Pb. The properties mentioned above are discussed except for β decays. The first forbidden transitions of β decays are of crucial importance for describing the decay half-lives and delayed neutron emissions from heavy nuclei [16,17].

The present paper is organized as follows: In Sec. II, a brief description of the construction of the Hamiltonian is given. Section III presents the results of binding energies. The low-lying levels and core-excited properties, including the evolution of the $N = 126$ shell gap, are discussed in Secs. IV and V, respectively. Sections VI and VII present discussions on electric quadrupole and magnetic dipole properties, respectively. A summary is given in Sec. VIII.

II. SHELL-MODEL HAMILTONIAN

The present Hamiltonian is constructed in the model space with five proton orbits and thirteen neutron orbits. The five proton orbits, $0g_{7/2}$, $1d_{5/2}$, $1d_{3/2}$, $2s_{1/2}$, and $0h_{11/2}$, are named PO5 (five proton orbits) in the following discussions. The six neutron orbits below the $N = 126$ shell gap, $0h_{9/2}$, $1f_{7/2}$, $1f_{5/2}$, $2p_{3/2}$, $2p_{1/2}$, and $0i_{13/2}$, are named NO6 (six neutron orbits) in the following discussions. The seven neutron orbits above the $N = 126$ shell gap, $0i_{11/2}$, $1g_{9/2}$, $1g_{7/2}$, $2d_{5/2}$, $2d_{3/2}$, $3s_{1/2}$, and $0j_{15/2}$, are named NO7. The proton orbits above the $Z = 82$ shell gap are not included in the present work, except for the study of core-excited states in ^{208}Pb, where the six orbits beyond the $Z = 82$ shell gap are included, as discussed in Sec. V.

The single-particle energies of the present Hamiltonian are fixed to reproduce the single-particle levels of ^{207,209}Pb and ^{207}Tl, the proton separation energy of ^{208}Pb, and the neutron separation energies of ^{208,209}Pb [14,18].

The Hamiltonian KHHE [19] was constructed in the model space consisting of PO5 and NO6. KHHE is included in the present Hamiltonian for the proton-proton interaction inside PO5, the neutron-neutron interaction inside NO6, and the proton-neutron interaction between PO5 and NO6. KHHE is based on the Kuo-Herling hole (KHH) interaction [20,21]. As suggested in Ref. [22], proton-proton and proton-neutron interactions of KHH are modified to give more precise descriptions of the levels in nuclei around ^{208}Pb. The construction of KHHE included such modifications and further considered modifications on neutron-neutron interaction [19].

The Hamiltonian KHPE [23], which is based on Kuo-Herling particle (KHP) interaction [20,21], is constructed in the model space including six proton orbits beyond $Z = 82$ and NO7. Recently, KHPE was used to analyze the spin and parity of the newly observed nuclide ^{223}Np [24] and isomeric state of ^{218}Pa [25]. The neutron-neutron part of KHPE is used for the neutron-neutron interaction inside NO7 in the present Hamiltonian.

In the present Hamiltonian, the monopole-based universal interaction V_{MU} [26] and the spin-orbit force from M3Y [27] (V_{MU}+LS) are used for the proton-neutron interaction between PO5 and NO7 and the neutron-neutron interaction between NO6 and NO7. In addition, the V_{MU}+LS interaction is used to complete the Hamiltonian to study both the proton and neutron core excitations of ^{208}Pb. The V_{MU}+LS interaction was examined to be suitable for shell-model calculations in different regions, such as the psd region [28], $sdpf$ [29], $pfsdg$ region [30], the region southeast of ^{132}Sn [31], and the region northwest of ^{208}Pb [32,33]. It is employed as a unified nuclear force to construct Hamiltonians in model spaces around ^{132}Sn and ^{208}Pb. The root mean square (rms) deviation of excitation energy of more than 800 theoretical states is nearly 0.2 MeV [34,35].

Table I summarizes the construction of the Hamiltonian. Because the proton-proton interaction inside PO5 is from KHHE which includes the Coulomb interaction, the calculated binding energies do not need Coulomb correction. In addition, 0.1 MeV is added to all two-body matrix elements (TBMEs) of proton-proton interaction except $\langle 2s_{1/2}2s_{1/2} \mid V \mid$

TABLE I. Construction of the two-body part of the present Hamiltonian.

	Type of interaction	Source of interaction
PO5-PO5	proton-proton	KHHE (modified)
NO6-NO6	neutron-neutron	KHHE
NO7-NO7	neutron-neutron	KHPE
PO5-NO6	proton-neutron	KHHE
PO5-NO7	proton-neutron	V_{MU}+LS
NO6-NO7	neutron-neutron	V_{MU}+LS

$2s_{1/2}2s_{1/2}\rangle$. Such modification provides more precise descriptions of the binding energies of Au, Pt, and Ir isotopes, which will be discussed in Sec. III. The modification rarely affects the spectroscopic properties of Pb, Tl, and Hg isotopes, because the monopole effect is canceled in these isotopes when the single-particle energies of these proton orbits are fixed to those of ^{207}Tl.

Systematic shell-model calculations are challenging in the full medium and heavy mass region due to the huge computation dimension of most of the nuclei. As the computation consumption increases exponentially with the valence particles (holes), this work mainly focuses on the Pb, Tl, and Hg isotopes and the $A \geqslant 198$ nuclei, around the $N = 126$ shell. As for the nuclei around $A = 190$ whose properties have been experimentally measured, they are anticipated to be investigated through approximations, such as further truncation on the model space.

The consideration of core excitation also extends the computation dimension. Furthermore, considering the mixing between the normal states and the core-excited states would aggravate the case and introduces many complicated correlations. For example, if one neutron crossing $N = 126$ shell is considered, the diagonal TBMEs $\langle(PO5)(NO7)| V |(PO5)(NO7)\rangle$ and $\langle(NO6)(NO7)| V |(NO6)(NO7)\rangle$ should be included. But if the mixing between the normal states and the core-excited states are considered, more off-diagonal TBMEs $\langle(PO5)(NO6)| V |(PO5)(NO7)\rangle$ and $\langle(NO6)(NO6)| V |(NO6)(NO7)\rangle$ should be considered. Besides, the properties and strength of the off-diagonal cross-shell interaction have been rarely studied. It is shown that a weaker off-diagonal cross-shell interaction can reproduce the low-lying properties of ^{14}C in a $4\hbar\omega$ calculation [36]. But it is more complicated in heavy nuclei because there are orbits with three major shell differences, such as $0g_{7/2}$ and $0j_{15/2}$ orbits. As a result, except for the study of ^{208}Pb, only one-neutron excitation across the $N = 126$ shell gap is considered for core-excited states in the present work.

III. BINDING ENERGIES

Nuclear mass or binding energy is one of the most fundamental properties of an atomic nucleus. Many global mass models are available, such as the liquid drop (LD) model [37], finite-range droplet model [38], the Lublin-Strasbourg drop model [39], the Hartree-Fock-Bogoliubov model [40,41], and the Weizsäcker-Skyrme mass model [42,43]. The overall uncertainties of the global mass models are around 0.5 MeV. The

recent version of the Weizsäcker-Skyrme mass model includes the surface diffuseness effect for the extremely neutron-rich nuclei, where the neutrons may extend very far beyond the core [43]. The investigation on the neutron-halo nucleus, ^{22}C, shows that its predicted radius is strongly affected by the neutron-neutron interaction between the two valence neutrons and the configurations of the ^{20}C core [44]. There are some local mass models, which predict the unknown mass of a nucleus with high precision from the masses of the nearby nuclei, such as the Garvey-Kelson relations [45] with generalizations [46] and some new suggestions [47].

Although the nuclear shell model is more often used to study the spectroscopic properties rather than the bulk properties, it can provide a precise description of masses or binding energies if the Hamiltonian is adequately tuned. Because the shell-model calculations are performed with a core, the calculated binding energy of a specific nucleus is the sum of the observed binding energy of the core and the shell-model binding energy of this nucleus relative to the core.

As shown in Table II, the binding energies calculated through the Hamiltonian described in Sec. II, labeled as BE_{SM}, are compared with the observed data. The 56 experimental binding energies are well reproduced by the shell-model calculations with an rms deviation of only 0.134 MeV. Such a description is much more precise than the global mass models and comparable with the local mass models. In general, the nuclei close to ^{208}Pb are more precisely reproduced. Based on the present Hamiltonian, some unmeasured binding energies are predicted in Table III for neutron-rich Pb, Tl, Hg, Au, Pt, Ir, Os, Re, and W isotopes. For Ir, Os, Re, and W isotopes, only results of $N = 123$, 124, 125, 126, and 127 isotones are presented because of the enormous computational cost for other isotones. In general, the present Hamiltonian provides similar predictions to those of AME2020, with an rms deviation of 0.294 MeV. Future mass measurements of these nuclei can further constrain the shell-model Hamiltonian.

If the proton-proton interaction is not modified, all binding energies of nuclei with $Z < 80$, $^{198-203}$Au, $^{198-202}$Pt, and ^{199}Ir, are overbound compared with the observed data, which are presented in the Appendix. The effect of the interaction modification is not apparent in the calculation of Pb, Tl, and Hg isotopes, because all proton orbits except $2s_{1/2}$ are almost fully occupied in these isotopes and their effect on binding energies is canceled when the single-particle energies are fitted to those of ^{207}Tl. During the construction of the KHHE interaction, the experimental data of the Au, Pt, and Ir isotopes were not used for the fit. When the Au, Pt, and Ir isotopes are considered, the proton holes in other orbits contribute to the binding energies. Thus the proton $1d_{3/2}$, $1d_{5/2}$, $0g_{7/2}$, and $0h_{11/2}$ orbits are modified in the present work.

The observed and calculated one-neutron separation energies (S_n) are presented in Fig. 1 for Pb, Tl, Hg, Au, Pt, Ir, Os, Re, and W isotopes. The present Hamiltonian almost exactly reproduces the observed S_n values, including the odd-even staggering. The S_n values show strong similarity among nine isotopes both above and below the $N = 126$ shell gap, which indicates that the dominated neutron configurations are similar among these nuclei, as discussed in Sec. IV. Even in the neutron-rich Ir, Os, Re, and W isotopes around $N = 126$,

TABLE II. The comparison between the calculated and observed binding energies (units in MeV). Experimental data are taken from the 2020 atomic mass evaluation (AME2020) [18]. The rms deviation between calculations and observations is for all 56 nuclei.

Nuclide	BE_{SM}	BE_{Expt}	ΔBE	Nuclide	BE_{SM}	BE_{Expt}	ΔBE	Nuclide	BE_{SM}	BE_{Expt}	ΔBE
^{215}Pb	1666.803	1666.839	0.036	^{211}Tl	1645.832	1645.756	−0.076	^{203}Hg	1601.067	1601.159	0.092
^{214}Pb	1663.220	1663.293	0.073	^{210}Tl	1640.891	1640.854	−0.037	^{202}Hg	1595.141	1595.164	0.023
^{213}Pb	1658.194	1658.241	0.047	^{209}Tl	1637.209	1637.180	−0.029	^{201}Hg	1587.349	1587.410	0.061
^{212}Pb	1654.466	1654.516	0.050	^{208}Tl	1632.220	1632.214	−0.006	^{200}Hg	1581.194	1581.179	−0.015
^{211}Pb	1649.367	1649.389	0.022	^{207}Tl	1628.427	1628.427	0.000	^{199}Hg	1573.149	1573.151	0.002
^{210}Pb	1645.522	1645.553	0.031	^{206}Tl	1621.582	1621.575	−0.007	^{198}Hg	1566.690	1566.487	−0.203
^{209}Pb	1640.368	1640.368	0.000	^{205}Tl	1615.071	1615.071	0.000	^{203}Au	1599.855	1599.816	−0.039
^{208}Pb	1636.430	1636.430	0.000	^{204}Tl	1607.518	1607.525	0.007	^{202}Au	1592.925	1592.954	0.029
^{207}Pb	1629.062	1629.062	0.000	^{203}Tl	1600.930	1600.869	−0.061	^{201}Au	1587.087	1586.930	−0.157
^{206}Pb	1622.323	1622.325	0.002	^{202}Tl	1593.021	1593.017	−0.004	^{200}Au	1579.783	1579.698	−0.085
^{205}Pb	1614.291	1614.238	−0.053	^{201}Tl	1586.283	1586.145	−0.138	^{199}Au	1573.279	1573.481	−0.248
^{204}Pb	1607.564	1607.506	−0.058	^{200}Tl	1578.049	1577.941	−0.108	^{198}Au	1566.108	1565.896	−0.212
^{203}Pb	1599.222	1599.112	−0.110	^{199}Tl	1571.142	1570.882	−0.260	^{202}Pt	1591.962	1592.075	0.113
^{202}Pb	1592.319	1592.195	−0.124	^{198}Tl	1562.569	1562.145	−0.290	^{201}Pt	1585.121	1585.052	−0.069
^{201}Pb	1583.648	1583.454	−0.194	^{208}Hg	1629.480	1629.512	0.032	^{200}Pt	1579.937	1579.840	−0.097
^{200}Pb	1576.602	1576.362	−0.240	^{207}Hg	1624.618	1624.662	0.044	^{199}Pt	1572.711	1572.558	−0.153
^{199}Pb	1567.569	1567.272	−0.297	^{206}Hg	1620.993	1621.049	0.056	^{198}Pt	1567.271	1567.002	−0.269
^{198}Pb	1560.423	1560.036	−0.387	^{205}Hg	1614.239	1614.320	0.081	^{199}Ir	1570.561	1570.351	−0.210
^{213}Tl	1654.249	1654.037	−0.212	^{204}Hg	1608.548	1608.651	0.103	rms			0.134

the predicted S_n values are larger than 2.5 MeV, which means that the neutron drip line is still very far from $N = 126$ at $Z = 74$.

Based on the excellent performance of the present Hamiltonian on the binding energies and separation energies, it is used to calculate the levels, cross-shell excitations, and electromagnetic properties of nuclei in the region south of ^{208}Pb in the following discussions.

IV. LOW-LYING LEVELS

The present Hamiltonian, with the modification on all $1d_{3/2}$, $1d_{5/2}$, $0g_{7/2}$, and $0h_{11/2}$ orbits, gives excitation energies in nice agreement with experimental values, including those of both low-lying and core-excited states, a prerequisite that the Hamiltonian can be used to predict isomers and shell closure around $N = 126$. It is not necessary to discuss all cal-

culated levels in the present work. Some states in neutron-rich Pb, Tl, and Hg isotopes are discussed in this section, which concentrates on possible isomeric states with small transition energies, such as the 8_1^+ states in ^{210,212,214,216}Pb, the $21/2_1^+$ and $27/2_1^+$ states in ^{211,213,215}Pb, and the $13/2_1^+$ and $17/2_1^+$ states in ^{209,211,213}Tl. The half-lives of these possible isomeric states will be discussed in Sec. VI.

A. ^{210,212,214,216}Pb

As seen in Fig. 2, all 8_1^+ states in neutron-rich even-even Pb isotopes, ^{210,212,214,216}Pb, are located just above the 6_1^+ states, leading to the isomerism of these 8_1^+ states with half-lives of hundreds of nanoseconds or several microseconds. The 8_1^+ states in ^{214,216}Pb are observed without exact decay energies to the 6_1^+ states. As discussed in Ref. [4], the energies of the 8_1^+ to 6_1^+ transitions in ^{214,216}Pb are assumed to be between

TABLE III. The predicted binding energies from the present Hamiltonian and AME2020 [18] (units in MeV).

| Nuclide	BE_{SM}	BE_{AME}	ΔBE	Nuclide	BE_{SM}	BE_{AME}	ΔBE	Nuclide	BE_{SM}	BE_{AME}	ΔBE
^{217}Pb	1675.141	1675.023	−0.118	^{206}Pt	1611.098	1610.920	−0.178	^{200}Os	1573.440	1573.400	−0.040
^{216}Pb	1671.749	1671.840	0.091	^{205}Pt	1606.562	1606.380	−0.182	^{199}Os	1567.141	1566.926	−0.215
^{212}Tl	1649.379	1649.360	−0.019	^{204}Pt	1603.291	1603.236	−0.055	^{198}Os	1562.529	1562.220	−0.309
^{211}Hg	1641.145	1640.947	−0.198	^{203}Pt	1597.105	1597.001	−0.104	^{202}Re	1575.202		
^{210}Hg	1637.801	1637.790	−0.011	^{204}Ir	1596.142	1595.892	−0.250	^{201}Re	1572.396		
^{209}Hg	1632.980	1632.917	−0.063	^{203}Ir	1593.038	1592.535	−0.503	^{200}Re	1567.081		
^{209}Au	1627.867	1627.274	−0.593	^{202}Ir	1587.182	1586.710	−0.472	^{199}Re	1562.566	1562.150	−0.416
^{208}Au	1623.296	1623.024	−0.272	^{201}Ir	1582.132	1581.870	−0.262	^{198}Re	1556.692	1556.478	−0.214
^{207}Au	1619.925	1619.568	−0.357	^{200}Ir	1575.699	1575.600	−0.099	^{201}W	1564.982		
^{206}Au	1615.346	1615.040	−0.306	^{198}Ir	1563.834	1563.606	−0.228	^{200}W	1562.421		
^{205}Au	1611.820	1611.300	−0.520	^{203}Os	1586.666	1586.242	−0.424	^{199}W	1557.215		
^{204}Au	1605.441	1605.072	−0.369	^{202}Os	1583.752	1583.478	−0.274	^{198}W	1553.076		
^{207}Pt	1614.225	1613.979	−0.246	^{201}Os	1578.066	1577.649	−0.417	^{197}W	1547.252	1547.041	−0.211
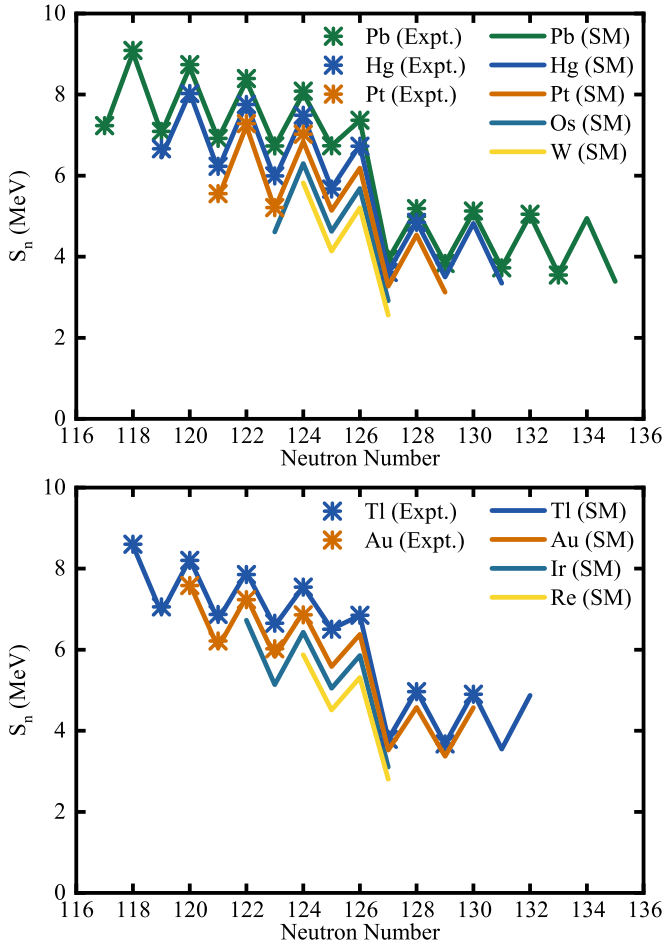
FIG. 1. The calculated and observed one-neutron separation energies of Pb, Hg, Pt, Os, and W (upper panel) and Tl, Au, Ir, and Re (lower panel) isotopes. Experimental data are taken from AME2020 [18].

FIG. 2. The calculated and observed levels of ^{210,212,214,216}Pb. Observed data are taken from NNDC [14]. The observed 8_1^+ states in ^{214,216}Pb are drawn 0.05 MeV above the corresponding 6_1^+ states as estimations. Dominant configurations of the 8_1^+ and 10_1^+ states and their percentages are indicated.

B. ^{211,213,215}Pb

In ^{211}Pb, the $21/2_1^+$ and $27/2_1^+$ states are located just above the $17/2_1^+$ and $23/2_1^+$ states, respectively, which are shown in Fig. 3. Both of them are observed as isomeric states with half-lives of around 100 ns. The shell-model results predict a similar tendency in ^{213,215}Pb.

The angular momenta of $17/2_1^+$ and $21/2_1^+$ are mainly from the coupling of three $\nu(1g_{9/2})$ neutrons, of which the maximum angular momentum is $21/2^+$. The angular momenta of $23/2_1^+$ and $27/2_1^+$ are mainly from the $\nu(1g_{9/2})^2(0i_{11/2})^1$ configuration, which can be considered as a $\nu(0i_{11/2})$ neutron coupled to the 8_1^+ and 6_1^+ states in the corresponding even Pb isotopes. Both $21/2_1^+$ and $27/2_1^+$ in ^{213,215}Pb are possible

0.02 and 0.09 MeV, which are drawn 0.05 MeV above the 6_1^+ states as estimations in Fig. 2.

The dominant configuration of 0_1^+, 2_1^+, 4_1^+, 6_1^+, and 8_1^+ in ^{210,212,214,216}Pb is $\nu(1g_{9/2})^n$, where n is the number of valence neutrons beyond the $N = 126$ shell gap. The configuration $\nu(1g_{9/2})^{n-2}(0i_{11/2})^2$ plays a more important role when the neutron number increases. Because the energy differences $E(4_1^+) - E(2_1^+)$, $E(6_1^+) - E(4_1^+)$, and $E(8_1^+) - E(6_1^+)$ stay almost constant among ^{210,212,214,216}Pb, these energy differences are mainly contributed by the coupling of two $\nu(1g_{9/2})$ neutrons.

The 10_1^+ state was observed in ^{210}Pb but not yet in ^{212,214,216}Pb. It is interesting to discuss how $E(10_1^+)$ varies when the neutron number increases. The calculations show $E(10_1^+)$ in ^{212,214,216}Pb are similar to that in ^{210}Pb and much larger than $E(8_1^+)$. The results indicate that the 10_1^+ states are not from the pure $\nu(1g_{9/2})$ configuration but the $\nu(1g_{9/2})^1(0i_{11/2})^1$ configuration. The neutron occupancies of the $\nu(1g_{9/2})$ orbit are 3.4, 4.8, and 6.1 in the 8_1^+ states of ^{212,214,216}Pb, respectively. Although many neutrons occupy this orbit, they do not tend to couple to an angular momentum 10.

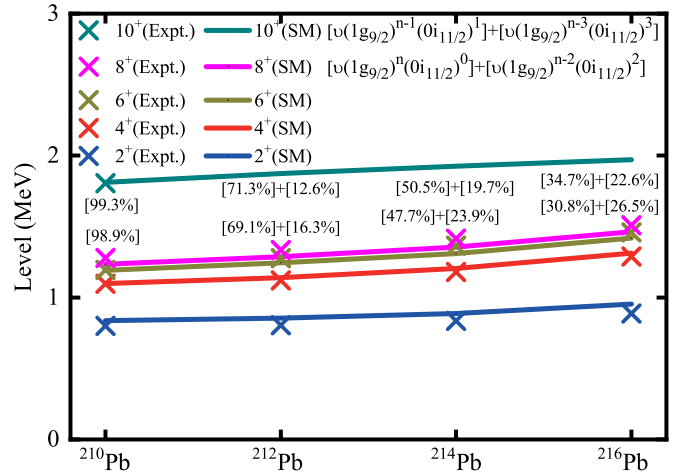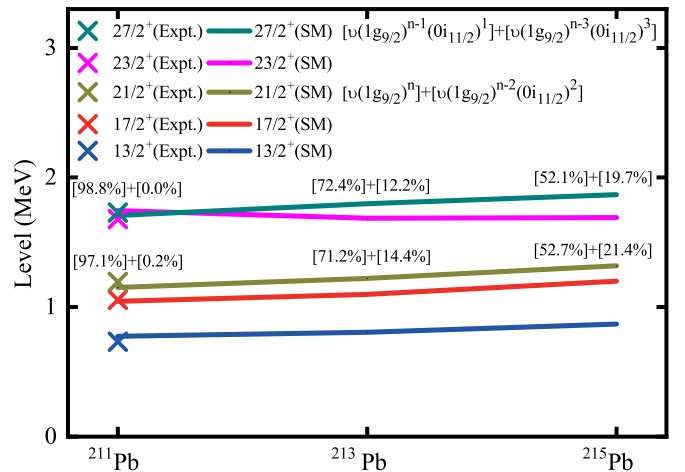FIG. 3. The calculated and observed levels of ^{211,213,215}Pb. Observed data are taken from NNDC [14]. The observed $27/2_1^+$ state in ^{211}Pb is drawn 0.05 MeV above the corresponding $23/2_1^+$ state as an estimation. Dominant configurations of the $21/2_1^+$ and $27/2_1^+$ states and their percentages are indicated.
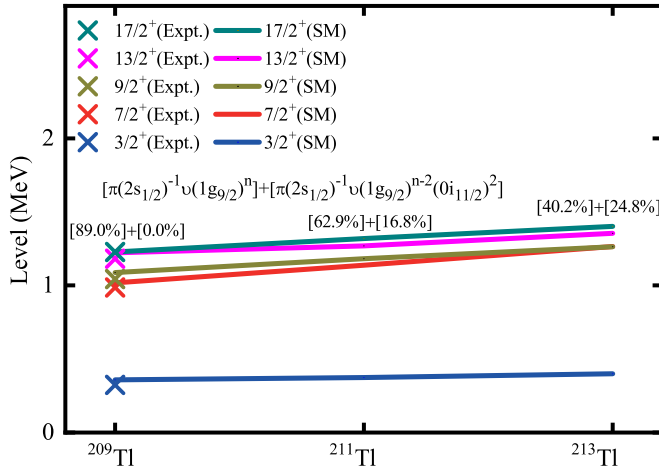
FIG. 4. The calculated and observed levels of ^{209,211,213}Tl. Observed data are taken from NNDC [14] and Ref. [48]. Dominant configurations of the $17/2_1^+$ states and their percentages are indicated.

FIG. 6. The calculated and observed levels of ^{206,208,210}Hg. Observed data are taken from NNDC [14]. The observed 8_1^+ states in ^{208,210}Hg are drawn 0.05 MeV above corresponding 6_1^+ states as estimations. Dominant configurations of the 8_1^+ and 10_1^+ states of ^{208,210}Hg and their percentages are indicated.

isomeric states through the present calculations. But the energy gaps between the $27/2_1^+$ and $23/2_1^+$ states become larger from ^{211}Pb to ^{215}Pb, which leads to shorter half-lives of the $27/2_1^+$ states.

C. ^{209,211,213}Tl

As shown in Fig. 4, the $17/2_1^+$ state is located just above the $13/2_1^+$ state and is an isomeric state in ^{209}Tl. The excitation energies are rather constant among ^{209,211,213}Tl. The $17/2_1^+$ and $13/2_1^+$ states in ^{211,213}Tl are possible isomeric states. All $9/2_1^+$, $13/2_1^+$, and $17/2_1^+$ states are dominated by the same configuration $\pi(2s_{1/2})^{-1}\nu(1g_{9/2})^2$, which can be considered as a $\pi(2s_{1/2})$ proton hole coupled to the 8_1^+ and 6_1^+ states in the corresponding Pb isotopes. The $9/2_1^+$ states are above the $7/2_1^+$ states in ^{209,211}Tl, which decay through

both $M1$ and $E2$ transitions. Although the $9/2_1^+$ state becomes lower than the $7/2_1^+$ state in ^{213}Tl, it is not predicted to be an isomeric state because there is a $5/2_1^+$ state at 0.4 MeV lower.

The present structure agrees well with the recent observed 0.58(8) μs isomer in ^{211}Tl [49], which suggests that the $17/2_1^+$ state is the isomer. Our prediction on the half-life of the $17/2_1^+$ state in ^{211}Tl is 0.65 μs, which will be shown in Sec. VI.

Two isomers deexciting with γ transitions of 380 and 698 keV, respectively, are found in ^{213}Tl [49]. Both the calculated positive-parity states in Ref. [49] and the present work do not seem to explain these two isomers. The isomer decaying via the 380-keV transition may correspond to the $11/2_1^-$ state with a proton $0h_{11/2}$ hole configuration. The $11/2_1^-$ state is
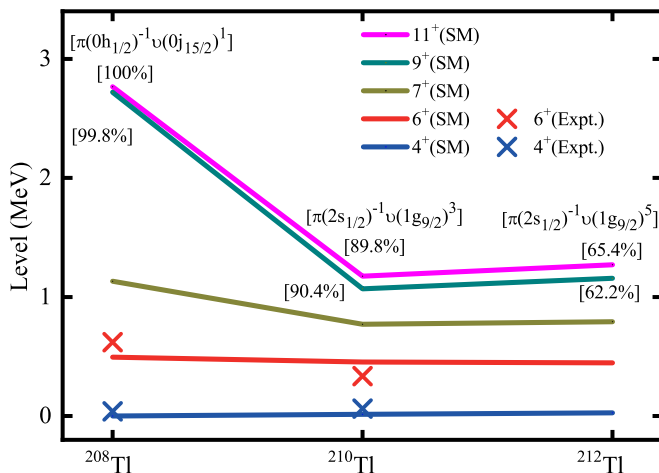

FIG. 5. The calculated and observed levels of ^{208,210,212}Tl. Observed data are taken from NNDC [14]. Dominant configurations of the 9_1^+ and 11_1^+ states and their percentages are indicated.
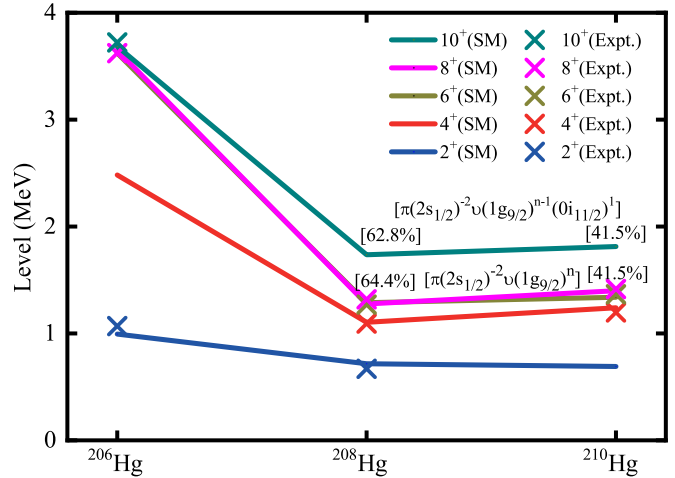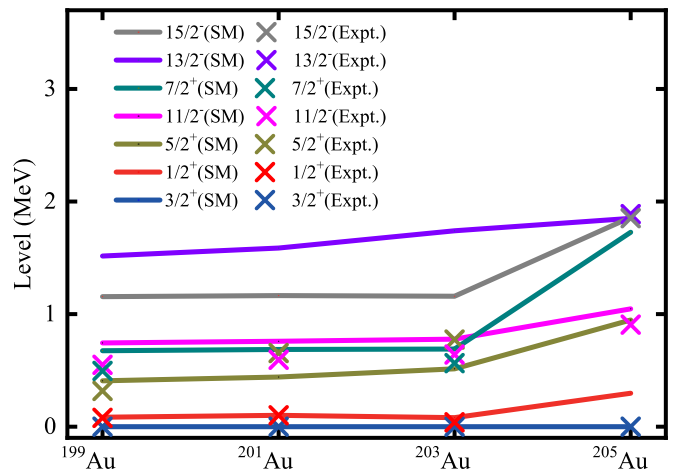

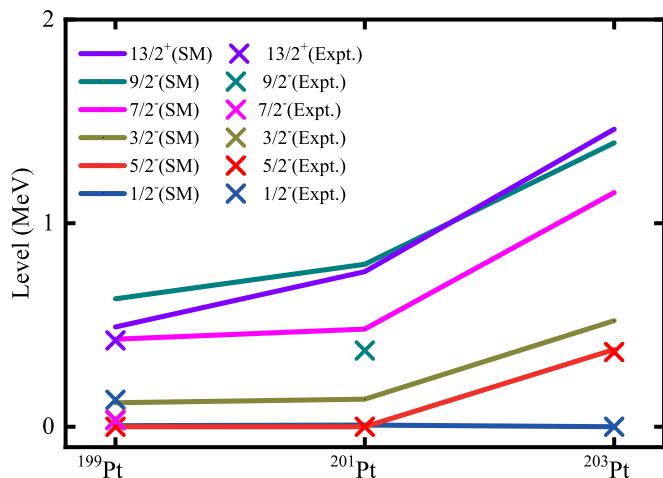FIG. 7. The calculated and observed levels of ^{199,201,203,205}Au. Observed data are taken from NNDC [14].

FIG. 8. The calculated and observed levels of ^{199,201,203}Pt. Observed data are taken from NNDC [14].

calculated to be just 10 keV above the $9/2_1^+$ state. Because of the uncertainty of calculation, $11/2_1^-$ may be actually below the $9/2_1^+$ state and decay to the $5/2_1^+$ state with decay energy 422 keV. The 698-keV γ line is rather weak and not discussed here.

D. ^{208,210,212}Tl

As shown in Fig. 5, the 11_1^+ and 9_1^+ states in ^{208}Tl are calculated to have high excitation energies, and they are dominated by the $\pi(0h_{11/2})^{-1}\nu(0j_{15/2})^1$ configuration. They can decay through $E1$ or $M1$ transitions to other states and are not isomeric states. The 9_1^- state (not drawn in Fig. 5) with the $\pi(0h_{11/2})^{-1}\nu(0g_{9/2})^1$ configuration is predicted to be an isomeric state, which is located 95 keV above the 7_1^+. Although
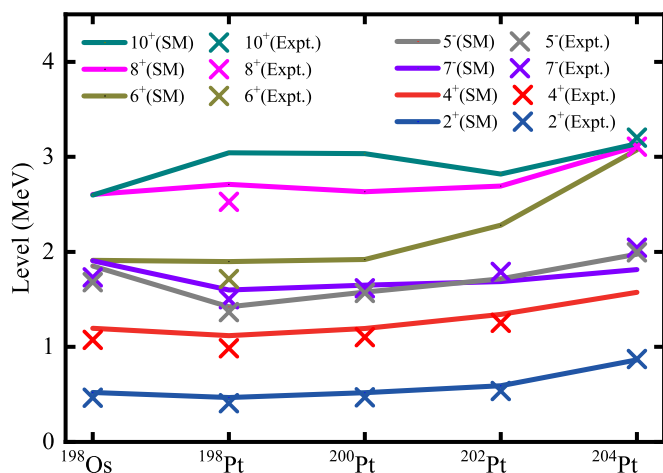
FIG. 9. The calculated and observed levels of ^{198}Os and ^{198,200,202,204}Pt. Observed data are taken from NNDC [14]. The observed 7_1^- states in ^{198}Os and ^{200,204}Pt are drawn 0.05 MeV above corresponding 5_1^- states as estimations. The observed 8_1^+ and 10_1^+ states in ^{204}Pt are drawn 0.05 MeV above 3.056 and 3.153 MeV, respectively.

the 12_1^+ state with the $\pi(0h_{11/2})^{-1}\nu(0j_{15/2})^1$ configuration is predicted below the 11_1^+ state, it can decay to the $10_{1,2}^-$ states through $M2$ transition with an estimated half-life around 10 ns.

The situation is different in ^{210,212}Tl. Because of more valence neutrons, the 11_1^+ and 9_1^+ states in ^{210,212}Tl are dominated by the $\pi(2s_{1/2})^{-1}\nu(1g_{9/2})^3$ configuration and located much lower than those in ^{208}Tl. The 11_1^+ states in ^{210,212}Tl are predicted to be isomeric in the present calculations. A possible high-spin β-decaying isomer is suggested to be the 11_1^+ state in ^{210}Tl [50], which will be discussed in Sec. VI. The 9_1^- states (not drawn in Fig. 5) in ^{210,212}Tl can decay to 9_1^+ states and are not predicted to be isomeric.

E. ^{206,208,210}Hg

From ^{206}Hg to ^{208}Hg, the excitation energies of the 6_1^+, 8_1^+, and 10_1^+ states are much reduced, as shown in Fig. 6.

FIG. 10. The calculated and observed levels of ^{206}Pb, ^{204}Pt, ^{202}Os, ^{200}W, and ^{198}Hf. Observed data are taken from Refs. [3,13,14,52].

FIG. 11. The same as Fig. 10 but for levels of ^{205}Au, ^{203}Ir, ^{201}Re, and ^{199}Ta.

FIG. 12. Effective single-particle energies of five proton orbits below the $Z = 82$ shell closures.

Such reduction indicates a transition from proton excitation to neutron excitation. The configurations of the 6_1^+, 8_1^+, and 10_1^+ states in ^{206}Hg are dominated by two proton holes in the $\pi(0h_{11/2})$ orbit. The 10_1^+ state is observed as an isomeric state above the 8_1^+ state. But the neutron excitations are dominant in the 6_1^+, 8_1^+, and 10_1^+ states in ^{208,210}Hg, which are similar to those of ^{210,212}Pb. The 8_1^+ states of ^{208,210}Hg were observed as isomeric states consistent with the present calculations.

F. Au, Pt, and Os isotopes

There are some recent experimental and theoretical works concerning the spectroscopic properties close to the $N = 126$ magic number below Hg isotopes. For example, proton-hole 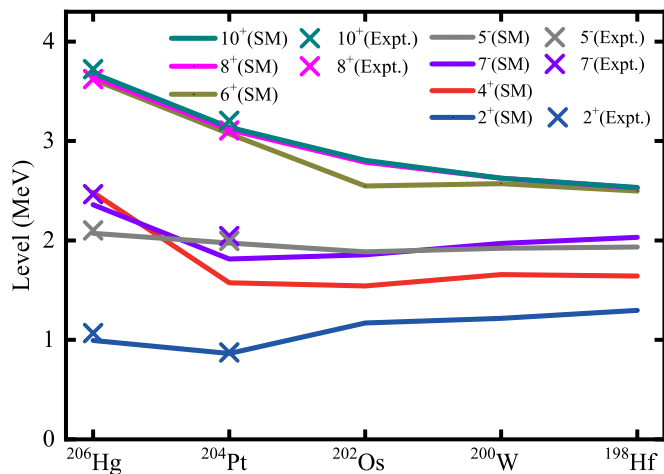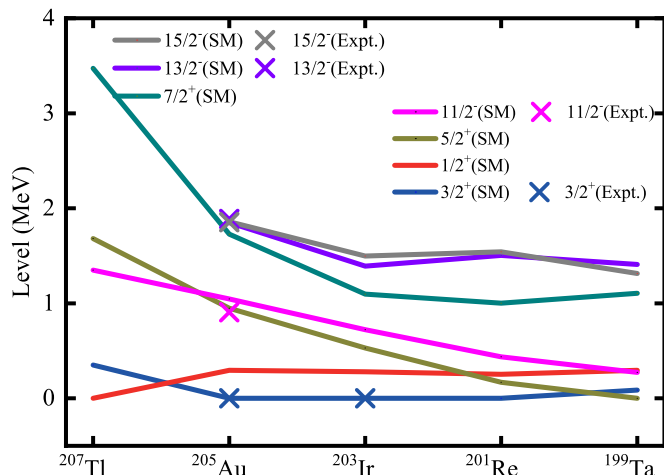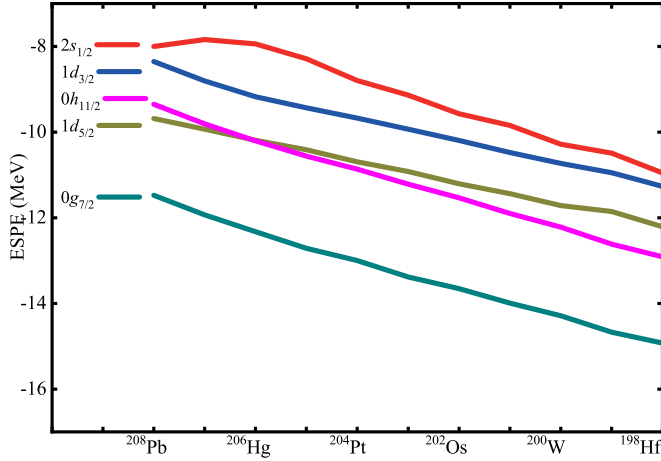states are observed in ^{205}Au, ^{204}Pt, and ^{203}Ir [3,13,51,52]. Recent observation of the ground-state band of ^{200}Pt shows that it is a transitional nucleus between the lighter Pt isotopes with γ-unstable properties and $N = 126$ nucleus ^{204}Pt with spherical shape [53]. Low-lying states in proton-hole isotopes
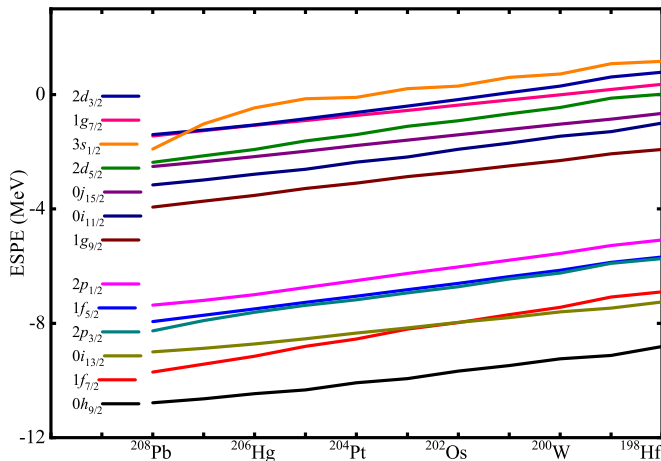

FIG. 13. Effective single-particle energies of six (seven) neutron orbits below (beyond) the $N = 126$ shell closures.

TABLE IV. The excitation energies of calculated and possible corresponding observed states in ^{208}Pb (units in MeV). The experimental data are taken from Ref. [14]. The configurations of the shell-model wave functions are also shown. Per_{SM} and Per_{ref} represent the configuration percentage calculated by the present work and by Ref. [60], respectively.

| J_{SM}^π	E_{SM}	J_{expt}^π	E_{expt}	Configuration	Per_{SM}	Per_{ref}
4_1^-	3.506	4_1^-	3.475	$\nu(2p_{1/2})^{-1}(1g_{9/2})^1$	98.4%	94.1%
5_1^-	3.247	5_1^-	3.198	$\nu(2p_{1/2})^{-1}(1g_{9/2})^1$	86.4%	90.3%
2_1^-	4.220	2_1^-	4.230	$\nu(1f_{5/2})^{-1}(1g_{9/2})^1$	89.1%	88.4%
3_2^-	4.127	3_2^-	4.051	$\nu(1f_{5/2})^{-1}(1g_{9/2})^1$	88.6%	90.3%
4_2^-	4.045	4_3^-	3.996	$\nu(1f_{5/2})^{-1}(1g_{9/2})^1$	96.0%	90.3%
5_2^-	3.860	5_2^-	3.709	$\nu(1f_{5/2})^{-1}(1g_{9/2})^1$	45.4%	39.7%
6_1^-	3.995	6_1^-	3.920	$\nu(1f_{5/2})^{-1}(1g_{9/2})^1$	98.9%	98.0%
7_1^-	3.819	7_1^-	4.037	$\nu(1f_{5/2})^{-1}(1g_{9/2})^1$	97.1%	98.0%
5_3^-	4.083	5_3^-	3.961	$\nu(2p_{1/2})^{-1}(0i_{11/2})^1$	40.9%	0.2%
				$\nu(1f_{5/2})^{-1}(1g_{9/2})^1$	37.9%	51.8%
6_2^-	4.225	6_2^-	4.206	$\nu(2p_{1/2})^{-1}(0i_{11/2})^1$	98.6%	94.1%
3_3^-	4.306	3_3^-	4.255	$\nu(2p_{3/2})^{-1}(1g_{9/2})^1$	56.7%	49.0%
4_4^-	4.351	4_5^-	4.359	$\nu(2p_{3/2})^{-1}(1g_{9/2})^1$	93.4%	65.6%
5_4^-	4.257	5_5^-	4.180	$\nu(2p_{3/2})^{-1}(1g_{9/2})^1$	71.9%	54.8%
6_3^-	4.407	6_4^-	4.481	$\nu(2p_{3/2})^{-1}(1g_{9/2})^1$	97.2%	86.5%
7_1^+	4.887	7_1^+	4.868	$\nu(2p_{1/2})^{-1}(0j_{15/2})^1$	89.5%	84.6%
8_1^+	4.729	8_1^+	4.611	$\nu(2p_{1/2})^{-1}(0j_{15/2})^1$	86.4%	60.8%
2_1^+	4.802			$\nu(0i_{13/2})^{-1}(1g_{9/2})^1$	90.9%	
3_1^+	5.017			$\nu(0i_{13/2})^{-1}(1g_{9/2})^1$	99.3%	
4_1^+	4.914	4_2^+	5.216	$\nu(0i_{13/2})^{-1}(1g_{9/2})^1$	94.7%	
5_1^+	5.028	5_1^+	5.193	$\nu(0i_{13/2})^{-1}(1g_{9/2})^1$	97.4%	
6_1^+	4.941	6_1^+	4.424	$\nu(0i_{13/2})^{-1}(1g_{9/2})^1$	85.1%	82.8%
7_2^+	5.059			$\nu(0i_{13/2})^{-1}(1g_{9/2})^1$	88.8%	
8_2^+	5.012	8_2^+	4.861	$\nu(0i_{13/2})^{-1}(1g_{9/2})^1$	88.3%	30.3%
9_1^+	5.049	9_1^+	5.010	$\nu(0i_{13/2})^{-1}(1g_{9/2})^1$	97.9%	96.0%
10_1^+	4.990	10_1^+	4.895	$\nu(0i_{13/2})^{-1}(1g_{9/2})^1$	71.9%	62.4%
11_1^+	5.088	(11_1^+)	5.235	$\nu(0i_{13/2})^{-1}(1g_{9/2})^1$	99.7%	
4_3^-	4.309	4_2^-	3.947	$\pi(2s_{1/2})^{-1}(0h_{9/2})^1$	89.6%	84.6%
5_5^-	4.354	5_6^-	4.297	$\pi(2s_{1/2})^{-1}(0h_{9/2})^1$	55.9%	4.0%
				$\nu(2p_{1/2})^{-1}(0i_{11/2})^1$	27.5%	29.2%
3_5^-	4.947	3_4^-	4.698	$\pi(1d_{3/2})^{-1}(0h_{9/2})^1$	40.2%	17.6%
				$\nu(1f_{5/2})^{-1}(0i_{11/2})^1$	49.6%	25.0%
4_5^-	4.599	4_4^-	4.262	$\pi(1d_{3/2})^{-1}(0h_{9/2})^1$	64.4%	62.4%
5_6^-	4.531	5_4^-	4.125	$\pi(1d_{3/2})^{-1}(0h_{9/2})^1$	71.3%	57.8%
6_4^-	4.678	6_3^-	4.383	$\pi(1d_{3/2})^{-1}(0h_{9/2})^1$	49.1%	86.5%
				$\nu(1f_{5/2})^{-1}(0i_{11/2})^1$	49.6%	0.0%
3_2^+	5.638			$\pi(0h_{11/2})^{-1}(0h_{9/2})^1$	59.6%	
4_2^+	5.771			$\pi(0h_{11/2})^{-1}(0h_{9/2})^1$	68.6%	
5_3^+	5.746			$\pi(0h_{11/2})^{-1}(0h_{9/2})^1$	57.0%	
6_4^+	5.741	6_2^+	5.213	$\pi(0h_{11/2})^{-1}(0h_{9/2})^1$	66.7%	82.8%
7_4^+	5.639	7_2^+	5.195	$\pi(0h_{11/2})^{-1}(0h_{9/2})^1$	56.9%	72.3%
8_4^+	5.653	8_3^+	5.093	$\pi(0h_{11/2})^{-1}(0h_{9/2})^1$	34.8%	34.8%
				$\nu(1f_{5/2})^{-1}(0j_{15/2})^1$	29.1%	25.0%
9_3^+	5.601	9_2^+	5.162	$\pi(0h_{11/2})^{-1}(0h_{9/2})^1$	69.9%	96.0%
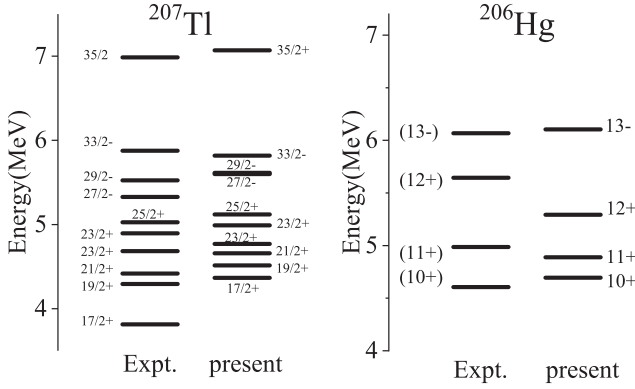
FIG. 14. The calculated and observed core-excited states in ^{207}Tl and ^{206}Hg. Observed data are taken from Refs. [14,15].

of Ir, Pt, Au, Hg, and Tl in the ^{208}Pb region are investigated through nucleon pair approximation, which agrees well with the observed data [54,55]. More nuclei below Hg isotopes should be studied in order to examine the ability of the present Hamiltonian.

As shown in Figs. 7, 8, and 9, the calculated energy levels of Au, Pt, and Os isotopes are in good agreement with the observed data. In particular, the differences between the calculated excitation energies of the $11/2_1^-$ states in $^{199-201}$Au and the corresponding experimental data are less than 0.2 MeV, which are around 0.4 MeV in Ref. [54]. Such improvement can be interpreted by the larger model space in the present

TABLE V. The configuration of the core-excited state in ^{207}Tl and ^{206}Hg, calculated with the present Hamiltonian.

Nuclide	State	Configuration	Percentage
^{207}Tl	$17/2_1^+$	$\pi(0h_{11/2})^{-1}\nu(2p_{1/2})^{-1}(1g_{9/2})^1$	82.4%
	$19/2_1^+$	$\pi(0h_{11/2})^{-1}\nu(2p_{1/2})^{-1}(1g_{9/2})^1$	82.4%
	$21/2_1^+$	$\pi(2s_{1/2})^{-1}\nu(0i_{13/2})^{-1}(1g_{9/2})^1$	71.7%
	$23/2_1^+$	$\pi(2s_{1/2})^{-1}\nu(0i_{13/2})^{-1}(1g_{9/2})^1$	79.9%
	$23/2_2^+$	$\pi(0h_{11/2})^{-1}\nu(1f_{5/2})^{-1}(1g_{9/2})^1$	81.8%
		$\pi(1d_{3/2})^{-1}\nu(0i_{13/2})^{-1}(1g_{9/2})^1$	10.3%
	$25/2_1^+$	$\pi(0h_{11/2})^{-1}\nu(1f_{5/2})^{-1}(1g_{9/2})^1$	81.4%
	$27/2_1^-$	$\pi(0h_{11/2})^{-1}\nu(0i_{13/2})^{-1}(1g_{9/2})^1$	98.8%
	$29/2_1^-$	$\pi(0h_{11/2})^{-1}\nu(0i_{13/2})^{-1}(1g_{9/2})^1$	98.6%
	$33/2_1^-$	$\pi(0h_{11/2})^{-1}\nu(0i_{13/2})^{-1}(1g_{9/2})^1$	99.5%
	$35/2_1^+$	$\pi(0h_{11/2})^{-1}\nu(0i_{13/2})^{-1}(0j_{15/2})^1$	100.0%
^{206}Hg	10_2^+	$\pi(2s_{1/2})^{-2}\nu(0i_{13/2})^{-1}(1g_{9/2})^1$	47.7%
		$\pi(1d_{3/2})^{-2}\nu(0i_{13/2})^{-1}(1g_{9/2})^1$	9.4%
		$\pi(0h_{11/2})^{-2}\nu(0i_{13/2})^{-1}(1g_{9/2})^1$	6.7%
	11_1^+	$\pi(2s_{1/2})^{-2}\nu(0i_{13/2})^{-1}(1g_{9/2})^1$	42.3%
		$\pi(1d_{3/2})^{-2}\nu(0i_{13/2})^{-1}(1g_{9/2})^1$	14.6%
		$\pi(0h_{11/2})^{-2}\nu(0i_{13/2})^{-1}(1g_{9/2})^1$	12.5%
	12_1^+	$\pi(2s_{1/2})^{-2}\nu(0i_{13/2})^{-1}(0i_{11/2})^1$	53.8%
		$\pi(1d_{3/2})^{-2}\nu(0i_{13/2})^{-1}(0i_{11/2})^1$	14.6%
		$\pi(0h_{11/2})^{-2}\nu(0i_{13/2})^{-1}(0i_{11/2})^1$	9.3%
	13_1^-	$\pi(2s_{1/2})^{-2}\nu(0i_{13/2})^{-1}(0j_{15/2})^1$	37.8%
		$\pi(1d_{3/2})^{-2}\nu(0i_{13/2})^{-1}(0j_{15/2})^1$	14.3%
		$\pi(0h_{11/2})^{-2}\nu(0i_{13/2})^{-1}(0j_{15/2})^1$	11.2%

TABLE VI. The predicted excitation energies of the lowest five one-neutron cross-shell excited states with different spins and parities in ^{205}Au, ^{204}Pt, ^{203}Ir, and ^{202}Os (units in MeV).

Nuclide	State	E_x	Nuclide	State	E_x
^{205}Au	$9/2^-$	2.837	^{203}Ir	$9/2^-$	2.726
	$11/2^-$	2.840		$7/2^-$	2.732
	$7/2^-$	2.970		$11/2^-$	2.744
	$13/2^-$	2.990		$13/2^-$	2.768
	$5/2^-$	3.196		$5/2^-$	2.835
	$13/2^+$	3.605		$13/2^+$	3.178
	$11/2^+$	3.621		$11/2^+$	3.198
	$15/2^+$	3.635		$15/2^+$	3.200
	$9/2^+$	3.664		$17/2^+$	3.236
	$17/2^+$	3.685		$9/2^+$	3.239
^{204}Pt	5^-	2.845	^{202}Os	5^-	2.706
	4^-	2.939		4^-	2.795
	6^-	3.219		6^-	3.107
	7^-	3.263		7^-	3.162
	3^-	3.357		3^-	3.237
	8^+	4.163		8^+	3.982
	7^+	4.192		7^+	4.029
	9^+	4.252		9^+	4.152
	6^+	4.253		6^+	4.161
	5^+	4.317		10^+	4.233

work. Though some calculation deviated from observed data up to 0.4 MeV, it should be noted that most spins and parities in these nuclei are not fully experimentally determined but with uncertainties. For instance, the ground-state spin of ^{199}Pt is certainly assigned $5/2_1^-$, supported by the systematics in the region and the $M1$ assignment to the 32 keV γ decay [56]. However, the 32- and 35.9-keV states in ^{199}Pt are uncertainly assigned to be $(7/2)^-$ and $(3/2)^-$ states, respectively. Deeper investigation on nuclei in the region south of ^{208}Pb is still needed. Overall, the present Hamiltonian is also helpful to
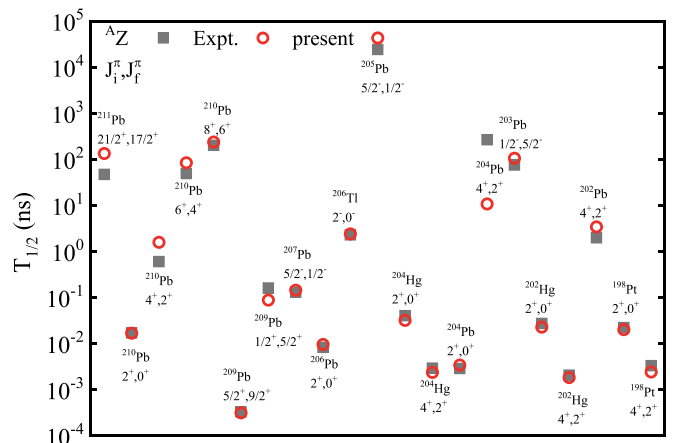

FIG. 15. The calculated and observed half-lives corresponding to $E2$ transitions. The calculated results are based on shell-model transition rates and observed transition energies. Observed data are taken from NNDC [14].

TABLE VII. The calculated and observed electric quadrupole moments Q (for the first 28 rows) or reduced transition strength $B(E2)$ (for the last 6 rows). Observed data are taken from Ref. [63]. M_p and M_n are proton and neutron $E2$ transition matrix elements, respectively. SM1 and SM2 are shell-model calculations with two sets of effective charges, $e_p = 1.57$, $e_n = 0.85$ and $e_p = 1.80$, $e_n = 0.80$, respectively. The units for E_x, Q, $B(E2)$, and M are keV, e b, e^2 b^2, and b, respectively. The rms deviation is calculated from Q and $\sqrt{(B(E2))}$.

Nuclide	E_x	J^π	M_p	M_n	Q_{SM1} or $B(E2)_{SM1}$	Q_{SM2} or $B(E2)_{SM2}$	Q_{expt} or $B(E2)_{\text{expt}}$
^{211}Pb	0	$9/2^+$	0.000	−0.217	−0.185	−0.174	+0.09(6)
^{209}Pb	0	$9/2^+$	0.000	−0.327	−0.278	−0.262	−0.27(17)
^{206}Pb	803	2^+	0.000	0.327	0.278	0.258	+0.05(9)
	2200	7^-	0.000	0.483	0.410	0.386	0.33(5)
	4027	12^+	0.000	0.551	0.469	0.441	[0.51(2)]
^{205}Pb	0	$5/2^-$	0.000	0.264	0.224	0.211	+0.23(4)
	1014	$13/2^+$	0.000	0.523	0.444	0.418	0.30(5)
	3196	$25/2^-$	0.000	0.706	0.600	0.565	0.63(3)
^{204}Pb	899	2^+	0.000	−0.043	−0.036	−0.034	+0.23(9)
	1274	4^+	0.000	0.347	0.295	0.277	0.44(2)
^{203}Pb	0	$5/2^-$	0.000	0.100	0.085	0.080	+0.10(5)
	1921	$21/2^+$	0.000	0.909	0.773	0.727	0.85(3)
^{202}Pb	2170	9^-	0.000	0.638	0.542	0.510	+0.58(9)
	2208	7^-	0.000	0.369	0.314	0.295	0.28(2)
^{201}Pb	0	$5/2^-$	0.000	−0.042	−0.035	−0.033	0.01(4)
	2719	$25/2^-$	0.000	0.512	0.435	0.410	0.46(2)
^{200}Pb	2154	7^-	0.000	0.414	0.352	0.332	0.32(2)
	2183	9^-	0.000	0.478	0.406	0.382	0.40(2)
	3006	12^+	0.000	0.589	0.501	0.471	0.79(3)
^{199}Pb	0	$3/2^-$	0.000	0.074	0.063	0.059	+0.08(9)
^{206}Hg	2102	5^-	0.381	0.000	0.598	0.684	0.74(15)
^{204}Hg	437	2^+	0.236	0.326	0.648	0.686	+0.4(2)
^{203}Hg	0	$5/2^-$	0.137	0.301	0.472	0.488	+0.344(7)
^{202}Hg	440	2^+	0.232	0.396	0.701	0.735	+0.87(13)
^{200}Hg	368	2^+	0.236	0.492	0.788	0.818	+0.96(11)
^{199}Hg	532	$13/2^+$	0.285	0.963	1.266	1.283	+1.2(3)
^{199}Au	0	$3/2^+$	0.183	0.324	0.563	0.589	+0.510(16)
^{198}Au	0	2^-	0.194	0.394	0.639	0.664	+0.640(19)
^{210}Pb	800	$B(E2; 0^+ \to 2^+)$	0.000	0.284	0.058	0.052	0.051(15)
^{206}Pb	803	$B(E2; 0^+ \to 2^+)$	0.000	0.373	0.100	0.089	0.0989(28)
^{204}Pb	899	$B(E2; 0^+ \to 2^+)$	0.000	0.470	0.160	0.142	0.1587(69)
^{204}Hg	437	$B(E2; 0^+ \to 2^+)$	0.258	0.357	0.509	0.562	0.424(21)
^{202}Hg	440	$B(E2; 0^+ \to 2^+)$	0.263	0.499	0.709	0.761	0.615(21)
^{200}Hg	368	$B(E2; 0^+ \to 2^+)$	0.265	0.611	0.884	0.931	0.855(28)
rms					0.123	0.126	

study the low-lying levels of Au and Pt isotopes around $N = 126$.

The excitation energies of all mentioned states increase significantly from ^{203}Au to ^{205}Au, since the proton configuration contributes more when the neutron number approaches 126. Similarly, the excitation energies of the yrast states in odd-A Pt isotopes increase with the neutron number.

G. $N = 126$ isotones below ^{206}Hg

Based on the previous discussions, the present Hamiltonian is also used to investigate levels of other nuclei in this region, such as the $N = 126$ isotones below Hg isotopes. The results from the present Hamiltonian are presented in Fig. 10 for even-even nuclei and in Fig. 11 for odd-even nuclei. On the whole, the present Hamiltonian generally reproduces well the

excited states in the $N = 126$ isotones above Ir isotopes. More spectroscopic studies, especially on the experimentally interesting nuclei ^{204}Pt, ^{202}Os, and ^{200}W, are necessary to verify the Hamiltonian.

The configurations and excitation energies of the yrast states along $N = 126$ isotones are very sensitive to the interaction related to the proton $1d_{3/2}$ orbit, which changes the gap between $1d_{3/2}$ and $2s_{1/2}$ orbits. As proton effective single-particle energies (ESPEs) presented in Fig. 12, with the modified proton-proton interaction, the $1d_{3/2}$ orbit becomes closer to the $2s_{1/2}$ orbit when the proton number decreases from ^{206}Hg.

Therefore, the present work provides a possible modification of the Hamiltonian, based on the available data of Au, Pt, and Ir isotopes. More data around and below Ir isotopes will be needed for reliable modification of the proton-proton interaction.

TABLE VIII. The prediction of possible isomers including transition energy (δE), $B(E2)$, and half-lives.

Nuclide	J_i^π	J_f^π	δE (MeV)	$B(E2)$ (e^2 fm^4)	Half-life (μs)
^{215}Pb	$17/2^+$	$13/2^+$	0.33	28.08	0.0047
	$21/2^+$	$17/2^+$	0.12	31.44	0.18
^{213}Pb	$17/2^+$	$13/2^+$	0.29	33.46	0.0069
	$21/2^+$	$17/2^+$	0.12	0.45	12.13
^{213}Tl	$13/2^+$	$9/2^+$	0.09	0.01	1812.75
	$17/2^+$	$13/2^+$	0.05	0.03	444.55
^{212}Tl	11^+	9^+	0.11	2.27	2.93
^{211}Tl	$13/2^+$	$9/2^+$	0.09	66.27	0.14
	$17/2^+$	$13/2^+$	0.05	18.66	0.65
^{210}Tl	11^+	9^+	0.11	140.76	0.053
^{210}Hg	6^+	4^+	0.10	69.26	0.12
	8^+	6^+	0.06	28.03	0.45
^{209}Hg	$17/2^+$	$13/2^+$	0.38	433.65	0.00016
	$21/2^+$	$17/2^+$	0.12	213.71	0.029

V. THE $N = 126$ SHELL GAP AND CROSS-SHELL EXCITATIONS

Based on the present Hamiltonian, the $N = 126$ shell gap and neutron core-excited states are discussed. Figure 13 presents the neutron ESPEs along $N = 126$ isotones, which are calculated through the present Hamiltonian with the shell-model occupancies. When the proton number decreases, the $N = 126$ gap keeps nearly constant with little quenching, and the relative positions of neutron orbits do not change much. Only neutron $1f_{7/2}$ and $0i_{13/2}$ orbits change their orders when proton number changes from 81 to 72.

In light and medium mass regions, the orders of some orbits dramatically change along isotopic or isotonic chains, leading to the disappearances of some traditional magic numbers and appearances of some new magic numbers. In the present heavy mass region, two possible mechanisms may be responsible for the little variation of the (sub)shell gaps. One reason is that the effective nucleon-nucleon interaction is relatively weaker in heavy nuclei because of the larger radius. Thus the effect on the (sub)shell gaps is generally less pronounced when a nucleon is removed or added. The other reason is the configuration mixing. The protons are first removed from the $2s_{1/2}$ orbit when proton number changes from 82 to 80. When the proton number further decreases,

TABLE IX. The estimation of unknown transition energies (δE) of isomeric states through observed half-lives and calculated $B(E2)$. Observed half-lives are taken from NNDC [14].

Nuclide	J_i^π	J_f^π	Half-life	$B(E2)$ (e^2 fm^4)	δE (MeV)
^{216}Pb	8^+	6^+	0.40(4)μs	14.97	0.12
^{214}Pb	8^+	6^+	6.2(3) μs	0.25	0.19
^{211}Pb	$27/2^+$	$23/2^+$	159(28) ns	66.83	0.10
^{209}Tl	$17/2^+$	$13/2^+$	95(11) ns	62.73	0.12
^{210}Hg	8^+	6^+	2(1) μs	28.03	0.01
^{208}Hg	8^+	6^+	99(14) ns	90.82	0.10
^{201}Pt	$19/2^+$	$15/2^+$	21(3) ns	1121.05	0.01

protons in $1d_{3/2}$, $1d_{5/2}$, and $0h_{11/2}$ orbits are almost simultaneously removed. Considering the shell evolution mechanism from the tensor force, $j = l + 1/2$ and $j = l - 1/2$ orbits have opposite contributions to ESPE [26,57,58]. For example, if $1d_{3/2}$ and $1d_{5/2}$ orbits are fully occupied or fully removed, their tensor interactions with other orbits are almost canceled and have no contributions to shell evolution. It is true that protons in $1d_{3/2}$ orbit are removed more quickly than those in $1d_{5/2}$ and $0h_{11/2}$ orbits; the latter two orbits are both $j = l + 1/2$ type orbits. However, because of the configuration mixing, the protons are removed from several orbits, which results in a cancellation of the contributions from the tensor interaction.

Based on the experimental data available in Ag and In isotopes, recent investigations on the $9/2_1^+$ and $1/2_1^-$ states in ^{123,125}Ag [12] and ^{101}In [59] show that the evolutions of the $Z = 40$ subshell are rather slow in Ag isotopes towards ^{132}Sn and in In isotopes towards ^{100}Sn, respectively. Shell-model calculations can well describe the shell evolution and spectroscopic properties in Ag and In isotopes through V_{MU}+LS interaction with slight modifications on the strength of the central force [12,59]. Therefore, more studies on isomeric states around $N = 126$ in the region south of ^{208}Pb would be rather helpful for further verification of the present Hamiltonian, especially for matrix elements and the configuration mixing between specific orbitals.

In addition to excitations inside one major shell, the observed core-excited states are also well described by the present work. For ^{208}Pb, only one-particle excitation across the $N = 126$ or $Z = 82$ shell gap is considered. Our results are compared with Ref. [60], which applied two to six single-particle single-hole configurations to reconstruct the wave functions of specific observed states. It is seen in Table IV that most excitation energies of low-lying states in ^{208}Pb can be well reproduced by the calculations. Moreover, the calculated configuration percentages of most states are in good agreement with those in Ref. [60]. On the whole, the cross-shell excitation part of the present Hamiltonian is generally suitable for ^{208}Pb.

It can be also indicated for ^{208}Pb that there are more low-lying states dominated by one-neutron cross-shell configurations than those by one-proton cross-shell configurations. The states below 4 MeV are likely dominated by one-neutron cross-shell configurations, except for the 4_2^- states. Such indication can be illustrated by comparing the energy levels and the shell gaps. It can be deduced with the observed binding energies of ^{208,209}Pb and ^{209}Bi [18] that the gap of $N = 126$ ($Z = 82$) and higher orbits is around 3.430 MeV (4.204 MeV). Therefore, the configuration mixing becomes important for states beyond 4 MeV. For example, the configuration mixing is rather strong in several 5^- states near 4 MeV.

In particular, more complicated configurations should be considered for states such as the 3_1^- and 2_1^+ states, which are hardly described by one-particle cross-shell configurations. The observed 3_1^- state in ^{208}Pb is well known for its collective octupole character with strong configuration mixing [61,62], which may be the reason that the percentages of dominating configuration in calculated 3_2^- and 3_3^- states are smaller than

TABLE X. Six sets of effective *g* factors (units in μ_n) with rms deviations between observed and calculated magnetic moments of 50 states of nuclei in the region south of ^{208}Pb. The rms deviation from free *g* factors is also presented for comparison. Set1 (Set3) is fitted to all 50 magnetic moments without (with) considering the $g_{p,n}^{(t)}$ terms. Also without considering $g_{p,n}^{(t)}$ terms, Set4 is fitted separately to 7 states in nuclei with $N \geqslant 126$ and 43 states in nuclei with $N < 126$. Set2 (Set5) is fitted to the same data set as Set1 (Set4) with considering the $g_{p,n}^{(t)}$ terms while the $g_{p,n}^{(l)}$ and $g_{p,n}^{(s)}$ terms are kept the same as Set1 (Set4). Set6 is fitted in a similar way as fitting Set4 but without consideration of $g_n^{(l)}$ term. Uncertainties of the fit parameters are indicated in parentheses.

	rms	$g_p^{(l)}$	$g_n^{(l)}$	$g_p^{(s)}$	$g_n^{(s)}$	$g_p^{(t)}$	$g_n^{(t)}$
Free	0.77	1	0	5.586	−3.826	0	0
Set1	0.20	1.033(0.023)	0.013(0.007)	3.735 (0.150)	−2.375 (0.113)	0	0
Set2	0.20	1.033(0.023)	0.013(0.007)	3.735 (0.150)	−2.375 (0.113)	0.369(0.199)	−0.046(0.074)
Set3	0.19	1.021(0.023)	0.004(0.011)	3.535 (0.166)	−2.029 (0.332)	0.591(0.254)	−0.291(0.245)
Set4	0.13						
($N \geqslant 126$)		1.030(0.005)	−0.072(0.071)	3.710 (0.043)	−2.386 (0.603)	0	0
($N < 126$)		1.022(0.019)	0.007(0.005)	3.770 (0.116)	−2.093 (0.084)	0	0
Set5	0.12						
($N \geqslant 126$)		1.030(0.005)	−0.072(0.071)	3.710 (0.043)	−2.386 (0.603)	0.100(0.072)	0.009(0.018)
($N < 126$)		1.022(0.019)	0.007(0.005)	3.770 (0.116)	−2.093 (0.084)	0.190(0.138)	−0.090(0.054)
Set6	0.13						
($N \geqslant 126$)		1.030(0.005)	0	3.728 (0.040)	−3.001 (0.020)	0	0
($N < 126$)		1.026(0.018)	0	3.757 (0.117)	−2.005 (0.056)	0	0

those in other states. The present work gives 2.746 MeV of the 3_1^- state with complicated mixing of both proton and neutron cross-shell configurations.

Overall, it should be noted that neutrons are easier to cross the major shell in the region south of ^{208}Pb, which is focused on in this work. Thus only one-neutron cross-shell configurations are considered for other nuclei in this section. Figure 14 shows that the core-excited states of ^{207}Tl and ^{206}Hg are well reproduced by the calculations with one-neutron cross-shell excitation. This indicates that the cross-shell interaction is reasonable up to $Z = 80$. The $17/2^+$ state in ^{207}Tl is also a collective octupole state with $\pi(0h_{11/2})^{-1}$ coupled to the 3_1^- state in ^{208}Pb, which is the reason that the excitation energy of the calculated state with simple configuration has large discrepancy with the experimental data.

Detailed configurations of these states are listed in Table V. Although the ground state of ^{207}Tl is dominated by a proton hole in the $2s_{1/2}$ orbit, many core-excited states have a proton hole in the $0h_{11/2}$ orbit, which contributes to the high angular momenta of these states.

Comparing with the shell-model calculations with KHH7B interaction [15], the present results give quite similar configurations for core-excited states (except for the $23/2_2^+$ state) in ^{207}Tl. For the $23/2_2^+$ state in ^{207}Tl, the present work gives a dominant $\pi(0h_{11/2})^{-1}\nu(1f_{5/2})^{-1}(1g_{9/2})^1$ configuration, while KHH7B interaction gives a strong configuration mixing between $\pi(0h_{11/2})^{-1}\nu(1f_{5/2})^{-1}(1g_{9/2})^1$ and $\pi(1d_{3/2})^{-1}\nu(0i_{13/2})^{-1}(1g_{9/2})^1$ configurations [15].

Contrary to ^{207}Tl, the angular momenta of observed core-excited states in ^{206}Hg are mostly originated from the coupling of neutrons. Two proton holes in the $2s_{1/2}$ orbit are dominant proton configuration and have no contribution to the angular momenta of these states. In addition the core-excited states in nuclei discussed above, ^{208}Pb, ^{207}Tl, and ^{206}Hg, the $1/2_1^-$ state in ^{209}Pb is well reproduced by a state with 65.6% $\nu(2p_{1/2})^{-1}(1g_{9/2})^2$, 18.5% $\nu(2p_{1/2})^{-1}(0i_{11/2})^2$, and 9.6% $\nu(2p_{1/2})^{-1}(0i_{11/2})^2$ configurations. The observed and calculated excitation energies are 2.149 and 2.219 MeV, respectively.

Some predictions are shown in Table VI for the excitation energies of the five lowest one-neutron cross-shell excited states with different spins and parities in ^{205}Au, ^{204}Pt, ^{203}Ir, and ^{202}Os. The spin parities of the calculated lowest states are quite similar between ^{204}Pt and ^{202}Os and between ^{205}Au and ^{203}Ir, respectively. But it becomes more difficult to find such cross-shell excited states when the proton number decreases. With more proton holes, normal states without cross-shell excitations are easier to have different spins and parities, while cross-shell excited states have fewer probabilities of being observed as yrast states.

VI. ELECTRIC QUADRUPOLE PROPERTIES

Generally speaking, effective charges are larger with a heavier core in shell-model calculations, because a heavier core normally has a stronger core polarization effect. For example, proton (neutron) effective charges are around 1.25 (0.25) for *psd* shell calculations with ^{4}He core [28], and 1.7 (0.7) for nuclei around ^{132}Sn [31]. However, for nuclei around ^{208}Pb, there are few investigations, especially systematic investigation, on the values of effective charges.

In the present study, 28 quadrupole moments and 6 $B(E2)$ values in Pb and Hg isotopes are considered to investigate the values of effective charges. If proton and neutron effective charges e_p and e_n are constrained as $e_p = 1 + e_n$, their values are 1.80 and 0.80 from fitting to the 34 observed data values. If the fitting is free without any constraints, e_p and e_n are 1.57 and 0.85, respectively. The values of effective charges obtained with the $e_p = 1 + e_n$ relationship are a little larger for the present ^{208}Pb region compared with those for the ^{132}Sn region.

TABLE XI. The calculated and observed 50 magnetic moments used in fitting. Observed data are taken from Refs. [69,70]. l_p (l_n), s_p (s_n), and t_p (t_n) are the proton (neutron) orbital angular momentum, spin, and tensor part of the nuclear matrix elements, respectively. Set1, Set2, Set3, Set4, and Set5 are shell-model calculations with six sets of effective g factors listed in Table X. The unit for magnetic moments is μ_N.

	Nuclide	J^π	l_p	l_n	s_p	s_n	t_p	t_n	free	Set1	Set2	Set3	Set4	Set5	Set6	Expt.
$N \geqslant 126$	^{211}Pb	$9/2^+$	0.00	4.02	0.00	0.48	0.00	0.37	−1.83	−1.08	−1.10	−1.06	−1.43	−1.43	−1.44	1.4037(8)
	^{210}Pb	6^+	0.00	5.38	0.00	0.62	0.00	0.48	−2.35	−1.39	−1.41	−1.37	−1.86	−1.85	−1.85	1.87(9)
	^{210}Pb	8^+	0.00	7.17	0.00	0.83	0.00	0.65	−3.18	−1.87	−1.90	−1.84	−2.50	−2.49	−2.49	2.50(6)
	^{209}Pb	$9/2^+$	0.00	4.00	0.00	0.50	0.00	0.36	−1.91	−1.13	−1.15	−1.10	−1.48	−1.48	−1.50	1.4735(16)
	^{208}Tl	5^+	0.05	3.98	0.47	0.50	−0.25	0.36	0.76	0.67	0.56	0.46	0.31	0.29	0.31	+0.292(13)
	^{207}Tl	$1/2^+$	0.00	0.00	0.50	0.00	0.00	0.00	2.79	1.87	1.87	1.77	1.86	1.86	1.86	+1.876(5)
	^{206}Hg	5^-	4.89	0.00	0.11	0.00	0.03	0.00	5.51	5.47	5.48	5.40	5.45	5.45	5.45	+5.45(5)
$N < 126$	^{207}Pb	$1/2^-$	0.00	0.67	0.00	−0.17	0.00	−0.67	0.64	0.40	0.44	0.54	0.35	0.41	0.50	0.592583(9)
	^{207}Pb	$5/2^-$	0.00	2.86	0.00	−0.36	0.00	−0.57	1.37	0.89	0.91	0.90	0.77	0.82	0.72	+0.80(3)
	^{206}Pb	7^-	0.00	6.79	0.00	0.21	0.00	−0.19	−0.79	−0.40	−0.39	−0.33	−0.39	−0.37	−0.41	−0.152(3)
	^{206}Pb	12^+	0.00	11.08	0.00	0.92	0.00	0.74	−3.53	−2.04	−2.08	−2.04	−1.86	−1.93	−1.85	−1.80(2)
	^{205}Pb	$5/2^-$	0.00	2.83	0.00	−0.33	0.00	−0.58	1.28	0.83	0.86	0.86	0.72	0.77	0.67	+0.7117(4)
	^{205}Pb	$13/2^+$	0.00	6.02	0.00	0.48	0.00	0.41	−1.84	−1.06	−1.08	−1.07	−0.97	−1.00	−0.96	−0.98(4)
	^{205}Pb	$25/2^-$	0.00	11.92	0.00	0.58	0.00	0.18	−2.20	−1.21	−1.22	−1.17	−1.13	−1.14	−1.15	−0.845(14)
	^{205}Pb	$33/2^+$	0.00	15.23	0.00	1.27	0.00	1.02	−4.86	−2.81	−2.86	−2.81	−2.56	−2.65	−2.54	−2.44(8)
	^{203}Pb	$5/2^-$	0.00	2.82	0.00	−0.32	0.00	−0.58	1.21	0.79	0.81	0.82	0.68	0.73	0.63	+0.6864(5)
	^{203}Pb	$25/2^-$	0.00	12.10	0.00	0.40	0.00	0.12	−1.52	−0.78	−0.79	−0.79	−0.75	−0.77	−0.80	−0.74(4)
	^{202}Pb	9^-	0.00	8.89	0.00	0.11	0.00	−0.14	−0.41	−0.14	−0.13	−0.14	−0.17	−0.15	−0.21	−0.2276(7)
	^{202}Pb	16^+	0.00	15.68	0.00	0.32	0.00	0.04	−1.23	−0.55	−0.55	−0.60	−0.57	−0.57	−0.64	−0.67(16)
	^{202}Pb	19^-	0.00	18.17	0.00	0.83	0.00	0.50	−3.17	−1.72	−1.74	−1.75	−1.61	−1.66	−1.66	−1.88(6)
	^{201}Pb	$5/2^-$	0.00	2.80	0.00	−0.30	0.00	−0.58	1.15	0.75	0.78	0.79	0.65	0.70	0.60	+0.6753(5)
	^{201}Pb	$25/2^-$	0.00	12.10	0.00	0.40	0.00	0.11	−1.53	−0.79	−0.79	−0.79	−0.76	−0.77	−0.80	−0.79(4)
	^{201}Pb	$29/2^-$	0.00	14.00	0.00	0.50	0.00	0.21	−1.90	−0.99	−1.00	−1.01	−0.95	−0.97	−1.00	−1.011(6)
	^{200}Pb	7^-	0.00	6.76	0.00	0.24	0.00	0.01	−0.91	−0.47	−0.47	−0.46	−0.45	−0.45	−0.48	−0.21(10)
	^{200}Pb	9^-	0.00	8.88	0.00	0.12	0.00	−0.14	−0.45	−0.16	−0.15	−0.16	−0.19	−0.17	−0.23	−0.258(9)
	^{200}Pb	12^+	0.00	11.14	0.00	0.86	0.00	0.76	−3.31	−1.90	−1.94	−1.93	−1.74	−1.80	−1.73	−1.849(12)
	^{205}Tl	$1/2^+$	−0.08	0.11	0.47	0.00	0.01	−0.01	2.51	1.65	1.66	1.57	1.67	1.67	1.67	+1.63821461(12)
	^{205}Tl	$5/2^+$	0.19	1.87	0.45	−0.01	0.19	−0.07	2.73	1.92	1.99	1.94	1.91	1.96	1.90	+2.0(3)
	^{205}Tl	$25/2^+$	4.96	6.89	0.50	0.15	0.38	−0.13	7.15	6.71	6.85	6.80	6.67	6.75	6.65	+6.80(10)
	^{204}Tl	2^-	0.19	2.20	−0.20	−0.19	−0.21	−0.31	−0.16	−0.04	−0.11	−0.13	−0.12	−0.14	−0.15	0.09(1)
	^{203}Tl	$1/2^+$	−0.05	0.07	0.47	0.01	0.01	−0.01	2.57	1.70	1.70	1.61	1.72	1.72	1.71	+1.62225787(12)
	^{203}Tl	$3/2^+$	1.27	0.53	−0.29	−0.01	−0.53	−0.02	−0.28	0.28	0.09	0.01	0.25	0.15	0.25	0.0(2)
	^{202}Tl	2^-	0.13	2.14	−0.14	−0.13	−0.14	−0.24	−0.16	−0.06	−0.10	−0.10	−0.11	−0.12	−0.14	0.06(1)
	^{202}Tl	7^+	0.05	6.02	0.45	0.48	0.26	0.39	0.74	0.68	0.76	0.74	0.79	0.81	0.79	+0.90(4)
	^{201}Tl	$1/2^+$	−0.04	0.06	0.47	0.01	0.01	−0.01	2.59	1.72	1.72	1.63	1.74	1.74	1.73	+1.605(2)
	^{200}Tl	2^-	0.05	1.99	−0.02	−0.02	−0.05	−0.10	−0.01	0.04	0.03	0.02	0.02	0.02	0.00	0.04(1)
	^{205}Hg	$1/2^-$	−0.03	0.69	0.00	−0.16	−0.01	−0.62	0.61	0.37	0.40	0.49	0.33	0.38	0.31	+0.60089(10)
	^{204}Hg	2^+	0.73	1.26	0.01	0.00	−0.05	−0.04	0.80	0.82	0.81	0.78	0.80	0.80	0.80	+0.9(2)
	^{203}Hg	$5/2^-$	0.19	2.63	0.00	−0.32	−0.01	−0.54	1.43	1.00	1.02	1.01	0.89	0.94	0.84	+0.84895(13)
	^{202}Hg	2^+	0.76	1.23	0.01	0.00	−0.04	−0.03	0.80	0.83	0.81	0.79	0.81	0.81	0.81	+0.78(6)
	^{202}Hg	4^+	1.12	2.85	0.02	0.01	−0.06	−0.07	1.18	1.23	1.21	1.18	1.21	1.20	1.19	1.4(3)
	^{201}Hg	$3/2^-$	0.03	1.07	0.00	0.40	0.00	0.12	−1.50	−0.91	−0.91	−0.81	−0.80	−0.81	−0.77	−0.5602257(14)
	^{200}Hg	2^+	0.73	1.25	0.01	0.01	−0.04	−0.03	0.74	0.78	0.76	0.75	0.76	0.76	0.76	+0.65(5)
	^{200}Hg	4^+	0.97	2.99	0.01	0.02	−0.05	−0.07	0.96	1.04	1.02	1.00	1.02	1.01	1.00	1.02(17)
	^{200}Au	12^-	4.98	6.06	0.48	0.48	0.36	0.40	5.83	5.88	6.00	5.94	5.94	5.97	5.96	5.90(9)
	^{199}Au	$3/2^+$	1.28	0.49	−0.27	0.00	−0.26	−0.01	−0.23	0.32	0.22	0.20	0.29	0.24	0.30	+0.261(2)
	^{198}Au	12^-	4.93	6.10	0.48	0.48	0.37	0.40	5.79	5.84	5.96	5.89	5.90	5.93	5.91	(+)5.83(9)
	^{198}Au	2^-	0.85	1.67	−0.26	−0.26	−0.21	−0.48	0.38	0.54	0.48	0.49	0.43	0.44	0.41	+0.5911(8)
	^{199}Pt	$5/2^-$	0.26	2.54	0.00	−0.30	−0.02	−0.52	1.43	1.03	1.05	1.04	0.92	0.97	0.88	+0.75(8)
	^{199}Pt	$13/2^+$	0.45	5.57	0.02	0.46	0.00	0.38	−1.21	−0.48	−0.50	−0.50	−0.40	−0.43	−0.39	−0.57(5)
RMS									0.74	0.20	0.20	0.19	0.13	0.12	0.13	

TABLE XII. The same as Table XI, but for magnetic moments with observed data not used in fitting. The results of both the first and second calculated states are presented for the corresponding states in $^{202-204}$Pb and ^{205}Tl.

Nuclide	J^{π}	l_p	l_n	s_p	s_n	t_p	t_n	Set1	Set2	Set3	Set4	Set5	Set6	Expt.
^{206}Pb	2^+	0.00	2.05	0.00	−0.05	0.00	−0.07	0.15	0.15	0.13	0.12	0.13	0.10	<0.03
^{204}Pb	2^+	0.00	2.04	0.00	−0.04	0.00	−0.12	0.11	0.12	0.12	0.09	0.10	0.07	<0.02
^{206}Tl	$(5)^+$	4.38	−0.18	0.48	0.33	0.37	0.43	5.54	5.66	5.60	5.60	5.64	5.65	+4.27(6)
^{204}Tl	$(7)^+$	0.07	6.01	0.45	0.48	0.27	0.39	0.69	0.77	0.75	0.80	0.81	0.79	+1.187(6)
^{203}Tl	$5/2^+$	0.27	1.76	0.46	0.01	0.19	−0.07	2.00	2.07	2.02	2.00	2.04	1.99	+2.6(11)
^{204}Pb	4^+	0.00	4.34	0.00	−0.34	0.00	−0.58	0.86	0.88	0.87	0.73	0.78	0.67	+0.225(4)
		0.00	4.11	0.00	−0.11	0.00	−0.64	0.33	0.36	0.44	0.27	0.33	0.23	+0.225(4)
^{203}Pb	$21/2^+$	0.00	10.45	0.00	0.05	0.00	−0.15	0.01	0.02	−0.02	−0.04	−0.03	−0.11	−0.64(2)
		0.00	10.17	0.00	0.33	0.00	−0.18	−0.64	−0.63	−0.57	−0.61	−0.60	−0.65	−0.64(2)
^{202}Pb	4^+	0.00	4.21	0.00	−0.21	0.00	−0.42	0.56	0.58	0.57	0.47	0.51	0.43	+0.008(16)
		0.00	4.13	0.00	−0.13	0.00	−0.81	0.37	0.41	0.52	0.31	0.38	0.27	+0.008(16)
^{205}Tl	$3/2^+$	1.20	0.60	−0.28	−0.02	−0.53	−0.02	0.23	0.04	−0.04	0.20	0.10	0.21	−0.8(5)
		0.44	1.15	−0.14	0.05	−0.37	0.03	−0.15	−0.29	−0.35	−0.16	−0.23	−0.16	−0.8(5)

The two sets of the effective charges obtained do not give a large difference in the results for the 34 observed $E2$ properties. The detailed results for the quadrupole moments and $B(E2)$ values are presented in Table VII. Almost all observed data are well reproduced by the shell-model transition matrix elements with the present two sets of effective charges. Although the calculations give the opposite sign for the quadrupole moments of the ground state of ^{211}Pb and the 2_1^+ state in ^{204}Pb, the absolute deviations from the experimental data are not large. Therefore, the theoretical results presented in Fig. 15, Table VIII, and Table IX are derived with $e_p = 1.80$ and $e_n = 0.80$.

The observed quadrupole moment of the ground state $(3/2^-)$ of ^{201}Hg is $+0.387(6)$ e b. Shell-model calculations fail to reproduce the $3/2^-$ state to be the ground state. The calculations give three very close $3/2^-$ states with excitation energies (quadrupole moments) 0.111 MeV (-0.07 e b), 0.170 MeV (0.09 e b), and 0.461 MeV (0.25 e b), respectively, where the quadrupole moments are calculated with $e_p = 1.80$ and $e_n = 0.80$. It seems that the third $3/2^-$ state is more likely to be the observed ground state because of its quadrupole moment. The magnetic moment of this $3/2^-$ state will be discussed in the Sec. VII.

Some observed $E2$ transition data are presented by half-lives instead of transition strengths. Because of uncertainties of the half-lives, they are not used to deduce the $B(E2)$ values and to fit effective charges. Some half-lives of nuclei in this region are calculated by shell-model transition rates and observed transition energies. It should be noted that electron conversion coefficients need to be considered when transition energies are small. The corresponding electron conversion coefficients are calculated by BRICC code from Australian National University [64].

It is seen in Fig. 15 that the half-lives are well reproduced, which means that the shell model provides reasonable transition rates. The only exception is the half-life of ^{204}Pb, of which the observed data is nearly 25 times longer than the calculation. In other words, the corresponding transition rate is around 25 times overestimated. As shown in Table VII, the $B(E2; 0^+ \rightarrow 2^+)$ value and the quadrupole moments

of the 4^+ state in ^{204}Pb are reasonably reproduced. The $B(E2; 2^+ \rightarrow 4^+)$ value seems unexpectedly overestimated by the shell-model calculation. But one should note that the absolute $B(E2; 2^+ \rightarrow 4^+)$ value evaluated from the half-life is only 0.52 e^2 fm^4, which is rather small and difficult to be exactly described.

Based on the reliable agreement between the observed and calculated $E2$ properties, some possible isomeric states, which decay through $E2$ transition with small decay energies, are presented in Table VIII with effective charges $e_p = 1.80$ and $e_n = 0.80$. The half-lives range from several nanoseconds to several microseconds.

Two isomeric states with rather long half-lives are predicted for $17/2^+$ and $13/2^+$ states in ^{213}Tl. The $17/2^+$, $13/2^+$, and $9/2^+$ states in ^{213}Tl are dominated by similar configurations, $\pi(2s_{1/2})^{-1}\nu(1g_{9/2})^6$ and $\pi(2s_{1/2})^{-1}\nu(1g_{9/2})^4(0i_{11/2})^2$. In the two transitions $17/2^+ \rightarrow 13/2^+$ and $13/2^+ \rightarrow 9/2^+$, the one-body transition densities involving $\nu(1g_{9/2})$ and $\nu(0i_{11/2})$ orbits are not large and greatly canceled by other components, which leads to small transition matrix elements. The experimental data of ^{213}Tl are rather limited [49], and these two predicted isomers are not found in a recent experiment.

The predicted half-life of the $17/2^+$ state in ^{211}Tl agrees quite well with the recently observed 0.58(8) μs isomer [49]. Reference [49] also suggested this isomer to be a $17/2^+$ state. Evidence was shown for a high-spin β-decaying isomer in ^{210}Tl [50]. The present calculation gives a 0.053-μs half-life for the 11_1^+ state, which is much smaller than the lower limit value of 3 μs of the β-decaying isomer [50]. If the 11_1^+ state is assumed to be a candidate for the β-decaying isomer, there are two possibilities. One possibility is that the decay energy from 11_1^+ to 9_1^+ is very small. For example, the half-life is estimated to be 2.7 μs when decay energy is 1.7 keV. Another possibility is that the 11_1^+ state is located below the 9_1^+ state and decays to other states with lower spins.

Based on the observed half-lives and calculated $E2$ properties, it is possible to estimate unknown transition energies of some isomeric states in the region south of Pb, such as transitions from 8_1^+ to 6_1^+ in ^{214,216}Pb and ^{208,210}Hg [14].

The estimated energies are rather small, which are listed in Table IX. The observed half-lives are given with fair uncertainties, which induce around 0.01 MeV uncertainties on the decay energies. The transition energies in ^{214,216}Pb are assumed to be between 0.02 and 0.09 MeV [4], which are slightly smaller than the present estimations. The present estimations provide reasonable information for future studies.

VII. MAGNETIC DIPOLE MOMENTS

Similar to the investigations on the effective charges, effective g factors are investigated based on 50 magnetic moments in this region. The $M1$ operator used in the present work includes six terms [65],

$$O(M1) = \sqrt{\frac{3}{4\pi}} \{ \overrightarrow{l}_p g_p^{(l)} + \overrightarrow{l}_n g_n^{(l)} + \overrightarrow{s}_p g_p^{(s)} + \overrightarrow{s}_n g_n^{(s)} $$
$$+ \sqrt{8\pi} [(Y_p^2 \otimes \overrightarrow{s}_p)^{(1)} g_p^{(t)} + (Y_n^2 \otimes \overrightarrow{s}_n)^{(1)} g_n^{(t)})] \}, \tag{1}$$

where $\overrightarrow{l}$, $\overrightarrow{s}$, and $Y^2 \otimes \overrightarrow{s}$ are the angular momentum, spin, and tensor terms of the operator, respectively, and $g_{p,n}^{(l)}$, $g_{p,n}^{(s)}$, and $g_{p,n}^{(t)}$ are corresponding proton and neutron g factors. For each term of the operator, the nuclear matrix element is calculated from the single-particle matrix element through the single-particle basis and the one-body transition density through the calculated shell-model wave functions. The magnetic moment is calculated through

$$\mu = g_p^{(l)} l_p + g_n^{(l)} l_n + g_p^{(s)} s_p + g_n^{(s)} s_n + g_p^{(t)} t_p + g_n^{(t)} t_n, \tag{2}$$

where $l_{p,n}$, $s_{p,n}$, and $t_{p,n}$ are the proton and neutron angular momentum, spin, and tensor terms of nuclear matrix elements, respectively.

Because shell-model calculations are performed in the truncated model space, effective g factors should be used instead of the free ones. In Table X, six sets of effective g factors are presented, which are fitted to the 50 magnetic moments listed in Table XI with the shell-model nuclear matrix elements. Set1 (Set3) of g factors is fitted to all 50 magnetic moments without (with) considering the $g_{p,n}^{(t)}$ terms. Also without considering the $g_{p,n}^{(t)}$ terms, Set4 of g factors is fitted separately to the 7 magnetic moments in nuclei with $N \geqslant 126$ and the 43 magnetic moments in nuclei with $N < 126$. Set2 (Set5) of g factors is fitted to the same data set as for Set1 (Set4) by considering the $g_{p,n}^{(t)}$ terms while the $g_{p,n}^{(l)}$ and $g_{p,n}^{(s)}$ terms are kept the same as those in Set1 (Set4). Set6 is fitted similarly as for Set4 but without considering the $g_n^{(l)}$ term. The rms deviations between the observed and calculated magnetic moments are also listed in Table X with the free g factors and the six sets of effective g factors for comparison. Comparing with the results with free g factors, all results from the six sets of effective g factors much reduce the rms deviations, which indicate strong core polarization effects on the g factors.

Any set of the effective g factors shown in Table XI successfully reproduces the experimentally observed 50 magnetic moments. It is reasonable to use them for further investigations on other magnetic moments and $M1$ transitions. The magnetic moments are generally sensitive to the
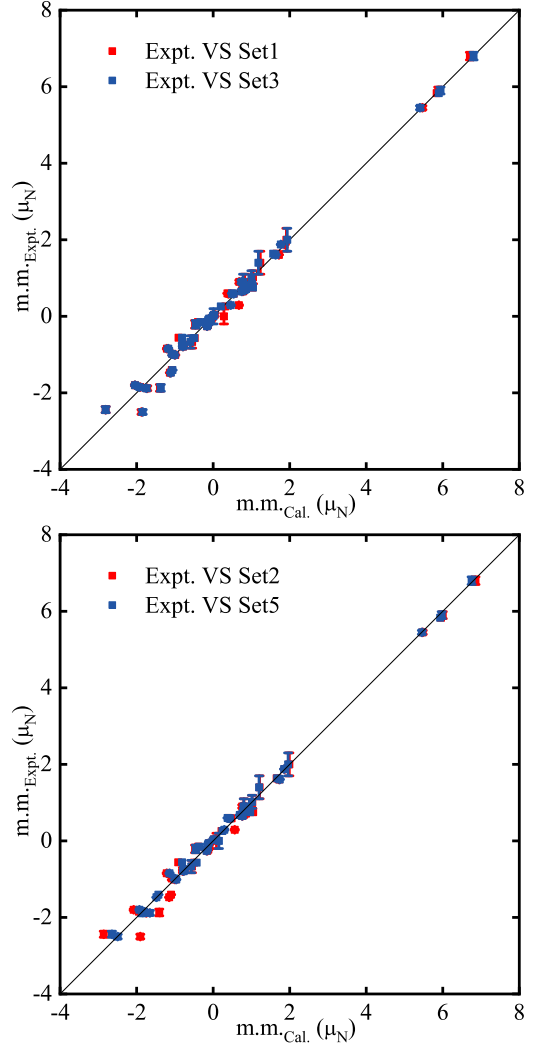

FIG. 16. The comparison between calculated and observed magnetic moments. Observed data are taken from Ref. [69].

single-particle configurations. The nice agreements between observed and calculated magnetic moments show that the present Hamiltonian reasonably accounts for the dominant configurations of considered states in Table XI.

As seen in Tables X and XI, total rms deviation and deviations between observed and calculated magnetic moments in $N \geqslant 126$ nuclei are much reduced if separate sets of effective g factors are used for magnetic moments with $N \geqslant 126$ and $N < 126$. The calculated magnetic moments with the effective g factors obtained from global fitting, Set1, Set2, and Set3, have certain deviations from the observations for the neutron-rich nuclei with $N \geqslant 126$, such as ^{209,210,211}Pb and ^{205}Tl shown worthwhile in Table XI. If the effective g factors are separately fitted for $N \geqslant 126$ and $N < 126$ nuclei, the results from Set4, Set5, and Set6 almost exactly reproduce the seven observed magnetic moments of ^{209,210,211}Pb, ^{205,207}Tl, and ^{206}Hg. Figure 16 presents a comparison between calculated results and observed data. The contribution of the $g^{(t)}$ term is so small that the Set1 results are similar to those of Set3 with the $g^{(t)}$ terms. After the separate consideration of

TABLE XIII. The same as Table XI, but for predicted magnetic moments without observed data.

Nuclide	J^π	l_p	l_n	s_p	s_n	t_p	t_n	Set1	Set2	Set3	Set4	Set5	Set6
^{217}Pb	$9/2^+$	0.00	4.08	0.00	0.42	0.00	0.38	−0.97	−0.97	−0.96	−1.31	−1.30	−1.27
^{215}Pb	$9/2^+$	0.00	4.06	0.00	0.44	0.00	0.38	−1.01	−1.01	−0.99	−1.34	−1.34	−1.32
^{213}Pb	$9/2^+$	0.00	4.04	0.00	0.46	0.00	0.37	−1.05	−1.06	−1.02	−1.39	−1.38	−1.38
^{216}Pb	8^+	0.00	7.26	0.00	0.74	0.00	0.68	−1.69	−1.69	−1.67	−2.29	−2.28	−2.22
^{214}Pb	8^+	0.00	7.23	0.00	0.77	0.00	0.67	−1.76	−1.77	−1.73	−2.36	−2.35	−2.31
^{212}Pb	8^+	0.00	7.20	0.00	0.80	0.00	0.66	−1.83	−1.84	−1.79	−2.43	−2.43	−2.40
^{213}Tl	$1/2^+$	−0.03	0.04	0.49	0.00	0.00	0.01	1.81	1.81	1.71	1.79	1.79	1.81
^{211}Tl	$1/2^+$	−0.03	0.04	0.49	0.00	0.00	0.01	1.81	1.81	1.71	1.79	1.79	1.80
^{209}Tl	$1/2^+$	−0.02	0.03	0.49	0.00	0.00	0.00	1.82	1.82	1.72	1.81	1.81	1.82
^{212}Tl	5^+	−0.01	4.07	0.49	0.45	−0.03	0.38	0.80	0.77	0.69	0.43	0.43	0.46
^{210}Tl	5^+	0.01	4.03	0.49	0.48	−0.13	0.37	0.74	0.66	0.59	0.38	0.37	0.39
^{209}Hg	$9/2^+$	0.04	3.99	0.00	0.47	0.01	0.36	−1.03	−1.04	−1.00	−1.38	−1.37	−1.38
^{207}Hg	$9/2^+$	0.04	3.96	0.00	0.50	0.01	0.36	−1.09	−1.10	−1.05	−1.43	−1.43	−1.45

$N \geqslant 126$ and $N < 126$ nuclei, the results with Set5 give a better agreement with the data compared with those of Set2. It is worthwhile to discuss the values of effective g factors to understand the origin of the difference.

In general, free $g^{(s)}$ factors should be quenched to reproduce the observed magnetic moments because of the core polarization effect. For the present results, quenching with factors of 63–68 % and 52–63 % (except that of Set6) are found for $g_p^{(s)}$ and $g_n^{(s)}$, respectively, which show stronger quenching comparing with those around 70% in the $f_{5/2}pg_{9/2}$-shell region [66], and around 90% in the sd-shell region [65] and psd-shell region [28]. It is reasonable that a larger core corresponds to a stronger core polarization effect and quenching.

All six sets of the effective g factors show a positive $\delta g_p^{(l)}$, defined as $g_{p,\mathrm{eff}}^{(l)} = g_{p,\mathrm{free}}^{(l)} + \delta g_p^{(l)}$, which is reasonable due to the meson exchange processes [67,68]. A negative $\delta g_n^{(l)}$, defined as $g_{n,\mathrm{eff}}^{(l)} = g_{n,\mathrm{free}}^{(l)} + \delta g_n^{(l)}$, is found with large uncertainty in the set of the effective g factors fitted to the magnetic moments with $N \geqslant 126$. The other sets of the effective g factors give a positive but tiny $\delta g_n^{(l)}$ except for Set6, which uses free $g_n^{(l)}$. For the magnetic moments with $N < 126$, a negative $\delta g_n^{(l)}$ increases the rms deviation dramatically. If $\delta g_n^{(l)} = -0.05$ is used for magnetic moments with $N < 126$ in Set4, the total rms deviation increases from 0.13 to 0.40.

Even if we use a free $g_n^{(l)}$ ($g_n^{(l)} = 0$), the present data are successfully reproduced and the rms deviation is reasonably small. If $g_n^{(l)} = 0$ is used in Set4 and other effective g factors are refitted, as shown for Set6 in Table X, the rms deviation nearly remains unchanged. In addition, all other effective g factors change little except for the $g_n^{(s)}$ factor for $N \geqslant 126$ nuclei: $g_n^{(s)}$ changes from $-2.386(0.603)\mu_n$ to $-3.001(0.020)\mu_n$, which is much different from that used for $N < 126$ nuclei. The different effective $g_n^{(s)}$ term for $N \geqslant 126$ and $N < 126$ nuclei is the main reason that the rms deviation is much reduced when the two situations are separately considered.

The contribution of the tensor term to the magnetic moments is rarely discussed. In the sd-shell region, the inclusion of the tensor terms changes little the total rms deviation between observed and calculated magnetic moments and $M1$ transitions [65]. The present work shows similar results that the inclusion of the tensor terms change the rms deviation little, as seen from Table X. The rms deviations are close to each other among Set1, Set2, and Set3, and between Set4 and Set5.

After separately considering the $N \geqslant 126$ and $N < 126$ nuclei, results are presented with free fitting of the $g^{(l)}$ and $g^{(s)}$ terms (Set4), with fitting of the $g^{(t)}$ terms when the $g^{(l)}$ and $g^{(s)}$ terms are fixed as Set4 (Set5), and with fitting of the $g^{(l)}$ and $g^{(s)}$ terms when the $g_n^{(l)}$ term is constrained to be zero (Set6). The results of free fitting of all the $g^{(l)}$, $g^{(s)}$, and $g^{(t)}$ terms are not presented, because there are only seven nuclei with $N \geqslant 126$, too few to fit six effective g factors. For $N < 126$ nuclei, the free fitting of all the $g^{(l)}$, $g^{(s)}$, and $g^{(t)}$ terms results in $g_n^{(s)} = -1.110(0.180)$ and $g_n^{(t)} = -0.768(0.130)$, which are quite different from those in the six sets and largely quenched from the free values, while the other four factors are not much different from those in the six sets. It seems the $g_n^{(t)}$ term substitutes partial effect of the $g_n^{(s)}$ term. Similar but less pronounced effects are found in Set3 and in the sd-shell region in Ref. [65]. It demands further and systematic investigations of the relationship between the $g_n^{(s)}$ and $g_n^{(t)}$ terms.

For the $3/2^-$ state in ^{201}Hg, unlike its quadrupole moment, the first calculated $3/2^-$ state gives the closest value of magnetic moment to the observed one, while the second and third calculated $3/2^-$ states have both positive magnetic moments. Considering that the quadrupole moment of the third calculated $3/2^-$ state mostly agrees with the experimental data, it is difficult to identify which calculated state corresponds to the observed ground state. Actually, configuration mixing is quite strong for the three calculated $3/2^-$ states, where the percentage of the largest component in these three states is less than 6%.

Some other experimental data on magnetic moments are available in this region in nuclei with $A \geqslant 200$. They are not discussed in Table XI but listed in Table XII. Some of these magnetic moments have no exact experimental values, such as the 2_1^+ states of ^{204,206}Pb, or uncertainties on spins, such

as the $(5)_1^+$ state of ^{206}Tl and the $(7)_1^+$ state of ^{204}Tl, or large uncertainty in observed value, such as the $5/2_1^+$ state of ^{203}Tl, or large deviation between observed and calculated values, such as the 4_1^+ states of ^{202,204}Pb, the $23/2_1^+$ state of ^{203}Pb, and the $3/2_1^+$ state of ^{205}Tl.

For magnetic moments of the 2_1^+ states of ^{204,206}Pb, the $(5)_1^+$ state of ^{206}Tl, the $(7)_1^+$ state of ^{204}Tl, and the $5/2_1^+$ state of ^{203}Tl, the present calculations provide reasonable results, which are not further discussed because of the lack of experimental information. As shown in Table XII, the calculated magnetic moments of the second corresponding states with the same spins and parities provide more reasonable descriptions of those of the 4_1^+ states of ^{202,204}Pb, the $23/2_1^+$ state of ^{203}Pb, and the $3/2_1^+$ state of ^{205}Tl. The corresponding yrare states locate not much higher than these yrast states. It is possible that the calculations do not reproduce the order of the yrast and yrare states because of the theoretical uncertainties.

The magnetic moment of the 3_1^- state in ^{208}Pb is $+1.9(2)\mu_N$ [69], and far from the calculated value, which is around $-0.8\mu_N$. Such deviation indicates that the present model space is not large enough for this 3^- state, which is considered to be a surface vibration state with octupole type [61,62] and needs to be described in a much larger model space. In general, it is difficult for the shell model to describe such octupole states, as discussed in Sec. V.

Based on the six sets of the effective g factors, magnetic moments of some neutron-rich Pb, Tl, and Hg isotopes are predicted in Table XIII. Because the nuclei in Table XIII are all with $N > 126$, magnetic moments predicted with

Set4, Set5, and Set6 are preferentially recommended. The values of magnetic moments of the ground states, $9/2^+$, of ^{211,213,215,217}Pb and ^{207,209}Hg are quite similar to each other, which are dominated by a single $1g_{9/2}$ neutron configuration. The $\nu(1g_{9/2})^2$, $\pi(2s_{1/2})^{-1}$, and $\pi(2s_{1/2})^{-1}\nu(1g_{9/2})^1$ configurations contribute dominantly to the magnetic moments of the 8_1^+ excited states of ^{210,212,214,216}Pb, the $1/2^+$ ground states of ^{207,209,211,213}Tl, and the 5^+ ground states of ^{208,210,212}Tl, respectively.

VIII. SUMMARY

In summary, shell-model investigations are performed for the region "south" of ^{208}Pb. The model space includes 5 proton orbits and 13 neutron orbits. The two-body matrix elements (TBMEs) are partly taken from the existing KHHE and KHPE Hamiltonians and partly calculated through the monopole-based universal interaction V_{MU} plus spin-orbit interaction. The newly constructed Hamiltonian can well reproduce binding energies, levels (including those of neutron core-excited states and isomeric states), and electric and magnetic properties of nuclei in the south proximity of ^{208}Pb (such as Pb, Tl, Hg, Au, and Pt isotopes around the $N = 126$ shell).

Based on the reasonable description of known properties, the present Hamiltonian predicts some unknown binding energies in nuclei around $N = 126$ and possible isomeric states in neutron-rich Pb, Tl, and Hg isotopes. The $N = 126$ shell closure is predicted to remain unchanged from $Z = 82$ to 72 with minor reduction of the gap.

TABLE XIV. The comparison between the calculated and observed binding energies (units in MeV). Experimental data are taken from AME2020 [18].

Nuclide	BE_{KHHE}	BE_{Ste11}	$BE_{present}$	BE_{Expt}	ΔBE_{KHHE}	ΔBE_{Ste11}	$\Delta BE_{present}$
^{208}Hg	1629.556	1629.552	1629.480	1629.512	−0.044	−0.040	0.032
^{207}Hg	1624.690	1624.687	1624.618	1624.662	−0.028	−0.025	0.044
^{206}Hg	1621.071	1621.071	1620.993	1621.049	−0.022	−0.022	0.056
^{205}Hg	1614.336	1614.330	1614.239	1614.320	−0.016	−0.010	0.081
^{204}Hg	1608.644	1608.627	1608.548	1608.651	0.007	0.024	0.103
^{203}Hg	1601.164	1601.144	1601.067	1601.159	−0.005	0.015	0.092
^{202}Hg	1595.241	1595.219	1595.141	1595.164	−0.077	−0.055	0.023
^{201}Hg	1587.449	1587.423	1587.349	1587.410	−0.039	−0.013	0.061
^{200}Hg	1581.297	1581.271	1581.194	1581.179	−0.118	−0.092	−0.015
^{199}Hg	1573.246	1573.213	1573.149	1573.151	−0.095	−0.062	0.002
^{198}Hg	1566.796	1566.769	1566.690	1566.487	−0.309	−0.282	−0.203
^{203}Au	1600.051	1600.020	1599.855	1599.816	−0.235	−0.204	−0.039
^{202}Au	1593.147	1593.097	1592.925	1592.954	−0.193	−0.143	0.029
^{201}Au	1587.296	1587.248	1587.087	1586.930	−0.366	−0.318	−0.157
^{200}Au	1580.001	1579.943	1579.783	1579.698	−0.303	−0.245	−0.085
^{199}Au	1573.946	1573.889	1573.729	1573.481	−0.465	−0.408	−0.248
^{198}Au	1566.332	1566.265	1566.108	1565.896	−0.436	−0.369	−0.212
^{202}Pt	1592.517	1592.390	1591.962	1592.075	−0.442	−0.315	0.113
^{201}Pt	1585.684	1585.547	1585.121	1585.052	−0.632	−0.495	−0.069
^{200}Pt	1580.513	1580.364	1579.937	1579.840	−0.673	−0.524	−0.097
^{199}Pt	1573.293	1573.135	1572.711	1572.558	−0.735	−0.577	−0.153
^{198}Pt	1567.860	1567.701	1567.271	1567.002	−0.858	−0.699	−0.269
^{199}Ir	1571.507	1571.294	1570.561	1570.351	−1.156	−0.943	−0.210
rms					0.443	0.358	0.129

We adopted the effective charges $e_p = 1.80$ and $e_n = 0.80$ for this mass region through the systematic investigations of 34 electric quadrupole properties. For magnetic dipole properties, it is recommended to use different sets of the effective g factors to calculate the magnetic moments of the $N \geqslant 126$ and $N < 126$ nuclei, while the reason is also clarified. If the tensor terms of the $M1$ operator are not taken into account as in many investigations, effective g factors, Set4 and Set6 in Table X (each includes two sets for the $N \geqslant 126$ and $N < 126$ nuclei, respectively), show reasonable agreement with the experimental values through the present studies of 50 magnetic moments.

Recently, many β-decay properties were measured in neutron-rich Au, Hg, Tl, Pb, and Bi isotopes, including decay half-lives, β delayed γ transitions, and neutron emissions [71–73]. It is expected that the present Hamiltonian can be used to investigate these β-decay properties, especially for nuclei around $N = 126$ shell closure. As discussed in previous works, the first-forbidden transitions in β decay are significant in the region south of ^{208}Pb [16,17]. A study based on the present Hamiltonian would be helpful for investigations on the r process, including both Gamow-Teller and first-forbidden transitions.

TABLE XV. The comparison between the calculated binding energies and binding energies predicted in AME2020 [18] (units in MeV).

Nuclide	BE$_{KHHE}$	BE$_{Ste11}$	BE$_{present}$	BE$_{AME}$	ΔBE$_{KHHE}$	ΔBE$_{Ste11}$	ΔBE$_{present}$
^{217}Pb	1675.141	1675.141	1675.141	1675.023	−0.118	−0.118	−0.118
^{216}Pb	1671.749	1671.749	1671.749	1671.840	0.091	0.091	0.091
^{212}Tl	1649.379	1649.379	1649.379	1649.360	−0.019	−0.019	−0.019
^{211}Hg	1641.215	1641.207	1641.145	1640.947	−0.268	−0.260	0.198
^{210}Hg	1637.875	1637.868	1637.801	1637.790	−0.085	−0.078	0.011
^{209}Hg	1633.051	1633.045	1632.980	1632.917	−0.134	−0.128	−0.063
^{209}Au	1628.037	1628.016	1627.867	1627.274	−0.763	−0.742	−0.593
^{208}Au	1623.455	1623.437	1623.296	1623.024	−0.431	−0.413	−0.272
^{207}Au	1620.096	1620.083	1619.925	1619.568	−0.528	−0.515	−0.357
^{206}Au	1615.499	1615.487	1615.346	1615.040	−0.459	−0.447	−0.306
^{205}Au	1611.996	1611.993	1611.820	1611.300	−0.696	−0.693	−0.520
^{204}Au	1605.657	1605.610	1605.441	1605.072	−0.585	−0.538	−0.369
^{207}Pt	1614.735	1614.615	1614.225	1613.979	−0.756	−0.636	−0.246
^{206}Pt	1611.613	1611.502	1611.098	1610.920	−0.693	−0.582	−0.178
^{205}Pt	1607.072	1606.967	1606.562	1606.380	−0.692	−0.587	−0.182
^{204}Pt	1603.812	1603.720	1603.291	1603.236	−0.576	−0.484	−0.055
^{203}Pt	1597.645	1597.542	1597.105	1597.001	−0.644	−0.541	−0.104
^{204}Ir	1597.002	1596.862	1596.142	1595.892	−1.110	−0.970	−0.250
^{203}Ir	1593.890	1593.768	1593.038	1592.535	−1.355	−1.233	−0.503
^{202}Ir	1588.082	1587.905	1587.182	1586.710	−1.372	−1.195	−0.472
^{201}Ir	1583.037	1582.860	1582.132	1581.870	−1.167	−0.990	−0.262
^{200}Ir	1576.617	1576.404	1575.699	1575.600	−1.017	−0.804	−0.099
^{198}Ir	1564.841	1564.552	1563.834	1563.606	−1.235	−0.946	−0.228
^{203}Os	1588.002	1587.683	1586.666	1586.242	−1.760	−1.441	−0.424
^{202}Os	1585.095	1584.814	1583.752	1583.478	−1.617	−1.336	−0.274
^{201}Os	1579.437	1579.125	1578.066	1577.649	−1.788	−1.476	−0.417
^{200}Os	1574.854	1574.505	1573.440	1573.400	−1.454	−1.105	−0.040
^{199}Os	1568.575	1568.180	1567.141	1566.926	−1.649	−1.254	−0.215
^{198}Os	1564.008	1563.594	1562.529	1562.220	−1.788	−1.374	−0.309
^{202}Re	1577.062	1576.531	1575.202				
^{201}Re	1574.248	1573.712	1572.396				
^{200}Re	1569.016	1568.506	1567.081				
^{199}Re	1564.531	1563.984	1562.566	1562.150	−2.381	−1.834	−0.416
^{198}Re	1558.718	1558.151	1556.692	1556.478	−2.240	−1.673	−0.214
^{201}W	1567.529	1566.871	1564.982				
^{200}W	1564.967	1564.325	1562.421				
^{199}W	1559.803	1559.132	1557.215				
^{198}W	1555.738	1555.065	1553.076				
^{197}W	1549.963	1549.258	1547.252	1547.041	−2.922	−2.217	−0.211
rms					1.244	0.998	0.294

APPENDIX

The calculated binding energies are listed in the Appendix for Hg, Au, Pt, Ir, Os, Re, and W isotopes based on three Hamiltonians, as shown in Tables XIV and XV. In addition the present results $BE_{present}$, results from two Hamiltonians, BE_{KHHE} and BE_{Ste11}, with the same proton-neutron and neutron-neutron parts are also presented to show the effect of the modification of the proton-proton interaction. BE_{KHHE} and BE_{Ste11} are calculated with the proton-proton interaction from the original KHHE and the modified one mentioned in

Ref. [3] (Ste11 means Steer *et al.*, 2011), respectively. The modifications in Ref. [3] aimed to give better descriptions on the proton-hole states of ^{205}Au and ^{203}Ir. As described in Sec. II, $BE_{present}$ are calculated with the proton-proton interaction from KHHE with 0.1 MeV added to interactions of $1d_{3/2}$, $1d_{5/2}$, $0g_{7/2}$, and $0h_{11/2}$ orbits, respectively. Because only the proton-proton interaction is different among these three Hamiltonians and the single-particle energies of ^{207}Tl are fixed to the observed data, all these Hamiltonians give the same results for Pb and Tl isotopes, which are already presented in Table II.

$BE_{present}$ are in good agreement with the 23 observed binding energies of Hg, Au, and Pt isotopes taken from AME2020 [18]. If the proton-proton interaction is not enlarged, binding energies of $^{198-203}$Au, $^{198-202}$Pt, and ^{199}Ir are overbound as in the BE_{KHHE} and BE_{Ste11} results compared with the observed data. It is also found that without the present modification, BE_{KHHE} and BE_{Ste11} generally present overbound results compared with those predicted by AME2020, especially when proton number becomes smaller. Because BE_{KHHE} and BE_{Ste11} overestimate the observed binding energies of Au and Pt isotopes, it is reasonable to assume that they also overestimate the unmeasured ones. $BE_{present}$ give more reasonable predictions compared with those in AME2020.

[1] M. R. Mumpower, R. Surman, G. C. McLaughlin, and A. Aprahamian, Prog. Part. Nucl. Phys. **86**, 86 (2016).

[2] T. Kajino and G. J. Mathews, Rep. Prog. Phys. **80**, 084901 (2017).

[3] S. J. Steer, Zs. Podolyák, S. Pietri, M. Górska, H. Grawe, K. H. Maier, P. H. Regan, D. Rudolph, A. B. Garnsworthy, R. Hoischen, J. Gerl, H. J. Wollersheim, F. Becker, P. Bednarczyk, L. Cáceres, P. Doornenbal, H. Geissel, J. Grębosz, A. Kelic, I. Kojouharov *et al.*, Phys Rev C **84**, 044313 (2011).

[4] A. Gottardo, J. J. Valiente-Dobón, G. Benzoni, R. Nicolini, A. Gadea, S. Lunardi, P. Boutachkov, A. M. Bruce, M. Górska, J. Grebosz, S. Pietri, Zs. Podolyák, M. Pfützner, P. H. Regan, H. Weick, J. Alcántara Núñez, A. Algora, N. Al-Dahan, G. de Angelis, Y. Ayyad *et al.*, Phys. Rev. Lett. **109**, 162502 (2012).

[5] A. Gottardo, J. J. Valiente-Dobón, G. Benzoni, A. Gadea, S. Lunardi, P. Boutachkov, A. M. Bruce, M. Górska, J. Grebosz, S. Pietri, Zs. Podolyák, M. Pfützner, P. H. Regan, H. Weick, J. Alcántara Núñez, A. Algora, N. Al-Dahan, G. de Angelis, Y. Ayyad, N. Alkhomashi *et al.*, Phys. Lett. B **725**, 292 (2013).

[6] H. Miyatake, M. Wada, X. Y. Watanabe, Y. Hirayama, P. Schury, M. Ahmed, H. Ishiyama, S. C. Jeong, Y. Kakiguchi, S. Kimura, J. Y. Moon, M. Mukai, M. Oyaizu, and J. H. Park, AIP Conf. Proc. **1947**, 020018 (2018).

[7] Y. X. Watanabe, Y. H. Kim, S. C. Jeong, Y. Hirayama, N. Imai, H. Ishiyama, H. S. Jung, H. Miyatake, S. Choi, J. S. Song, E. Clement, G. de France, A. Navin, M. Rejmund, C. Schmitt, G. Pollarolo, L. Corradi, E. Fioretto, D. Montanari, M. Niikura *et al.*, Phys. Rev. Lett. **115**, 172503 (2015).

[8] Y. Hirayama, M. Mukai, Y. X. Watanabe, M. Ahmed, S. C. Jeong, H. S. Jung, Y. Kakiguchi, S. Kanaya, S. Kimura, J. Y. Moon, T. Nakatsukasa, M. Oyaizu, J. H. Park, P. Schury, A.

Taniguchi, M. Wada, K. Washiyama, H. Watanabe, and H. Miyatake, Phys. Rev. C **96**, 014307 (2017).

[9] J. Chen, J. L. Lou, Y. L. Ye, Z. H. Li, D. Y. Pang, C. X. Yuan, Y. C. Ge, Q. T. Li, H. Hua, D. X. Jiang, X. F. Yang, F. R. Xu, J. C. Pei, J. Li, W. Jiang, Y. L. Sun, H. L. Zang, Y. Zhang, N. Aoi, E. Ideguchi *et al.*, Phys. Lett. B **781**, 412 (2018).

[10] J. Chen, J. L. Lou, Y. L. Ye, Z. H. Li, D. Y. Pang, C. X. Yuan, Y. C. Ge, Q. T. Li, H. Hua, D. X. Jiang, X. F. Yang, F. R. Xu, J. C. Pei, J. Li, W. Jiang, Y. L. Sun, H. L. Zang, Y. Zhang, G. Li, N. Aoi *et al.*, Phys Rev C **98**, 014616 (2018).

[11] R. Han, X. Q. Li, W. G. Jiang, Z. H. Li, H. Hua, S. Q. Zhang, C. X. Yuan, D. X. Jiang, Y. L. Ye, J. Li, Z. H. Li, F. R. Xu, Q. B. Chen, J. Meng, J. S. Wang, C. Xu, Y. L. Sun, C. G. Wang, H. Y. Wu, C. Y. Niu *et al.*, Phys. Lett. B **772**, 529 (2017).

[12] Z. Q. Chen, Z. H. Li, H. Hua, H. Watanabe, C. X. Yuan, S. Q. Zhang, G. Lorusso, S. Nishimura, H. Baba, F. Browne, G. Benzoni, K. Y. Chae, F. C. L. Crespi, P. Doornenbal, N. Fukuda, G. Gey, R. Gernhäuser, N. Inabe, T. Isobe, D. X. Jiang *et al.*, Phys. Rev. Lett. **122**, 212502 (2019).

[13] S. J. Steer, Zs. Podolyák, S. Pietri, M. Górska, P. H. Regan, D. Rudolph, E. Werner-Malento, A. B. Garnsworthy, R. Hoischen, J. Gerl, H. J. Wollersheim, K. H. Maier, H. Grawe, F. Becker, P. Bednarczyk, L. Cáceres, P. Doornenbal, H. Geissel, J. Grębosz, A. Kelic *et al.*, Phys. Rev. C **78**, 061302(R) (2008).

[14] http://www.nndc.bnl.gov/nudat3/.

[15] E. Wilson, Zs. Podolyák, H. Grawe, B. A. Brown, C. J. Chiara, S. Zhu, B. Fornal, R. V. F. Janssens, C. M. Shand, M. Bowry, M. Bunce, M. P. Carpenter, N. Cieplicka-Oryńczak, A. Y. Deo, G. D. Dracoulis, C. R. Hoffman, R. S. Kempley, F. G. Kondev, G. J. Lane, T. Lauritsen *et al.*, Phys. Lett. B **747**, 88 (2015).

[16] T. Suzuki, T. Yoshida, T. Kajino, and T. Otsuka, Phys. Rev. C **85**, 015802 (2012).

[17] N. Nishimura, Zs. Podolyák, D. L. Fang, and T. Suzuki, Phys. Lett. B **756**, 273 (2016).

[18] M. Wang, W. J. Huang, F. G. Kondev, G. Audi, and S. Naimi, Chin. Phys. C **45**, 030003 (2021).

[19] E. K. Warburton, Phys. Rev. C **44**, 233 (1991).

[20] T. T. S. Kuo and G. H. Herling, U.S. Naval Research Laboratory Report No. 2258, 1971 (to be published).

[21] G. H. Herling and T. T. S. Kuo, Nucl. Phys. A **181**, 113 (1972).

[22] L. Rydström, J. Blomqvist, R. J. Liotta, and C. Pomar, Nucl. Phys. A **512**, 217 (1990).

[23] E. K. Warburton and B. A. Brown, Phys. Rev. C **43**, 602 (1991).

[24] M. D. Sun, Z. Liu, T. H. Huang, W. Q. Zhang, J. G. Wang, X. Y. Liu, B. Ding, Z. G. Gan, L. Ma, H. B. Yang, Z. Y. Zhang, L. Yu, J. Jiang, K. L. Wang, Y. S. Wang, M. L. Liu, Z. H. Li, J. Li, X. Wang, H. Y. Lu *et al.*, Phys. Lett. B **771**, 303 (2017).

[25] M. M. Zhang, H. B. Yang, Z. G. Gan, Z. Y. Zhang, M. H. Huang, L. Ma, C. L. Yang, C. X. Yuan, Y. S. Wang, Y. L. Tian, H. B. Zhou, S. Huang, X. T. He, S. Y. Wang, W. Z. Xu, H. W. Li, X. X. Xu, J. G. Wang, H. R. Yang, L. M. Duan *et al.*, Phys. Lett. B **800**, 135102 (2020).

[26] T. Otsuka, T. Suzuki, M. Honma, Y. Utsuno, N. Tsunoda, K. Tsukiyama, and M. Hjorth-Jensen, Phys. Rev. Lett. **104**, 012501 (2010).

[27] G. Bertsch, J. Borysowicz, H. McManus, and W. G. Love, Nucl. Phys. A **284**, 399 (1977).

[28] C. Yuan, T. Suzuki, T. Otsuka, F. R. Xu, and N. Tsunoda, Phys Rev. C **85**, 064324 (2012).

[29] Y. Utsuno, T. Otsuka, B. A. Brown, M. Honma, T. Mizusaki, and N. Shimizu, Phys Rev. C **86**, 051301(R) (2012).

[30] T. Togashi, N. Shimizu, Y. Utsuno, T. Otsuka, and M. Honma, Phys Rev. C **91**, 024320 (2015).

[31] C. Yuan, Zhong Liu, Furong Xu, P. M. Walker, Zs. Podolyák, C. Xu, Z. Z. Ren, B. Ding, M. L. Liu, X. Y. Liu, H. S. Xu, Y. H. Zhang, X. H. Zhou, and W. Zuo, Phys. Lett. B **762**, 237 (2016).

[32] Z. Y. Zhang, H. B. Yang, M. H. Huang, Z. G. Gan, C. X. Yuan, C. Qi, A. N. Andreyev, M. L. Liu, L. Ma, M. M. Zhang, Y. L. Tian, Y. S. Wang, J. G. Wang, C. L. Yang, G. S. Li, Y. H. Qiang, W. Q. Yang, R. F. Chen, H. B. Zhang, Z. W. Lu *et al.*, Phys. Rev. Lett. **126**, 152502 (2021).

[33] H. B. Yang, Z. G. Gan, Z. Y. Zhang, M. H. Huang, L. Ma, M. M. Zhang, C. X. Yuan, Y. F. Niu, C. L. Yang, Y. L. Tian, L. Guo, Y. S. Wang, J. G. Wang, H. B. Zhou, X. J. Wen, H. R. Yang, X. H. Zhou, Y. H. Zhang, W. X. Huang, Z. Liu *et al.*, Phys Rev. C **105**, L051302 (2022).

[34] C. X. Yuan, Y. L. Ge, M. L. Liu, G. S. Chen, and B. S. Cai, EPJ Web Conf. **239**, 04002 (2020).

[35] C. X. Yuan and M. L. Liu (to be published).

[36] C. X. Yuan, Chin. Phys. C **41**, 104102 (2017).

[37] W. D. Myers and W. J. Swiatecki, Nucl. Phys. **81**, 1 (1966).

[38] P. Möller and J. R. Nix, At. Data Nucl. Data Tables **59**, 185 (1995).

[39] K. Pomorski and J. Dudek, Phys. Rev. C **67**, 044316 (2003).

[40] S. Goriely, N. Chamel, and J. M. Pearson, Phys. Rev. Lett. **102**, 152503 (2009).

[41] S. Goriely, N. Chamel, and J. M. Pearson, Phys. Rev. C **88**, 061302(R) (2013).

[42] M. Liu, N. Wang, Y. Deng, and X. Wu, Phys. Rev. C **84**, 014333 (2011).

[43] N. Wang, M. Liu, X. Z. Wu, and J. Meng, Phys. Lett. B **734**, 215 (2014).

[44] T. Suzuki, T. Otsuka, C. X. Yuan, and A. Navin, Phys. Lett. B **753**, 199 (2016).

[45] G. T. Garvey and I. Kelson, Phys. Rev. Lett. **16**, 197 (1966).

[46] Y. Y. Cheng, Y. M. Zhao, and A. Arima, Phys. Rev. C **90**, 064304 (2014).

[47] G. J. Fu, Y. Y. Cheng, Y. H. Zhang, P. Zhang, P. Shuai, Y. M. Zhao, and M. Wang, Phys. Rev. C **97**, 024339 (2018).

[48] B. M. S. Amro, C. J. Lister, E. A. McCutchan, W. Loveland, P. Chowdhury, S. Zhu, A. D. Ayangeakaa, J. S. Barrett, M. P. Carpenter, C. J. Chiara, J. P. Greene, J. L. Harker, R. V. F. Janssens, T. Lauritsen, A. A. Sonzogni, W. B. Walters, and R. Yanez, Phys. Rev. C **95**, 014330 (2017).

[49] A. Gottardo, J. J. Valiente-Dobón, G. Benzoni, A. I. Morales, A. Gadea, S. Lunardi, P. Boutachkov, A. M. Bruce, M. Górska, J. Grebosz, S. Pietri, Zs. Podolyák, M. Pfützner, P. H. Regan, D. Rudolph, H. Weick, J. Alcántara Núñez, A. Algora, N. Al-Dahan, G. de Angelis *et al.*, Phys. Rev. C **99**, 054326 (2019).

[50] R. Broda, L. W. Iskra, R. V. F. Janssens, B. A. Brown, B. Fornal, J. Wrzesiński, N. Cieplicka-Oryńczak, M. P. Carpenter, C. J. Chiara, C. R. Hoffman, F. G. Kondev, G. J. Lane, T. Lauritsen, Zs. Podolyák, D. Seweryniak, W. B. Walters, and S. Zhu, Phys. Rev. C **98**, 024324 (2018).

[51] Zs. Podolyák, G. F. Farrelly, P. H. Regan, A. B. Garnsworthy, S. J. Steer, M. Górska, J. Benlliure, E. Casarejos, S. Pietri, J. Gerl, H. J. Wollersheim, R. Kumar, F. Molina, A. Algora, N. Alkhomashi, G. Benzoni, A. Blazhev, P. Boutachkov, A. M. Bruce, L. Caceres *et al.*, Phys. Lett. B **672**, 116 (2009).

[52] Zs. Podolyák, S. J. Steer, S. Pietri, M. Górska, P. H. Regan, D. Rudolph, A. B. Garnsworthy, R. Hoischen, J. Gerl, H. J. Wollersheim, H. Grawe, K. H. Maier, F. Becker, P. Bednarczyk, L. Cáceres, P. Doornenbal, H. Geissel, J. Grebosz, A. Kelic, I. Kojouharov *et al.*, Eur. Phys. J. A **42**, 489 (2009).

[53] P. R. John, J. J. Valiente-Dobón, D. Mengoni, V. Modamio, S. Lunardi, D. Bazzacco, A. Gadea, C. Wheldon, T. R. Rodríguez, T. Alexander, G. de Angelis, N. Ashwood, M. Barr, G. Benzoni, B. Birkenbach, P. G. Bizzeti, A. M. Bizzeti-Sona, S. Bottoni, M. Bowry, A. Bracco *et al.*, Phys. Rev. C **95**, 064321 (2017).

[54] H. Jiang, J. J. Shen, Y. M. Zhao, and A Arima, J. Phys. G: Nucl. Part. Phys. **38**, 045103 (2011).

[55] H. Jiang and Y. M. Zhao, Sci. China Phys. Mech. Astron. **54**, 1461 (2011).

[56] B. Singh, Nucl. Data Sheets **108**, 79 (2007).

[57] T. Otsuka, R. Fujimoto, Y. Utsuno, B. A. Brown, M. Honma, and T. Mizusaki, Phys. Rev. Lett. **87**, 082502 (2001).

[58] T. Otsuka, T. Suzuki, R. Fujimoto, H. Grawe, and Y. Akaishi, Phys. Rev. Lett. **95**, 232502 (2005).

[59] X. Xu, J. H. Liu, C. X. Yuan, Y. M. Xing, M. Wang, Y. H. Zhang, X. H. Zhou, Yu. A. Litvinov, K. Blaum, R. J. Chen, X. C. Chen, C. Y. Fu, B. S. Gao, J. J. He, S. Kubono, Y. H. Lam, H. F. Li, M. L. Liu, X. W. Ma, P. Shuai *et al.*, Phys. Rev. C **100**, 051303(R) (2019).

[60] M. Rejmund, M. Schramm, and K. H. Maier, Phys. Rev. C **59**, 2520 (1999).

[61] A. M. Lane and E. D. Pendlebury, Nucl. Phys. **15**, 39 (1960).

[62] J. C. Carter, W. T. Pinkston, and W. W. True, Phys. Rev. **120**, 504 (1960).

[63] N. J. Stone, At. Data Nucl. Data Tables **111-112**, 1 (2016).

[64] T. Kibédi, T. W. Burrows, M. B. Trzhaskovskaya, P. M. Davidson, and C. W. Nestor, Jr., Nucl. Instrum. Methods A **589**, 202 (2008); http://bricc.anu.edu.au.

[65] W. A. Richter, S. Mkhize, and B. A. Brown, Phys. Rev. C **78**, 064302 (2008).

[66] M. Honma, T. Otsuka, T. Mizusaki, and M. Hjorth-Jensen, Phys. Rev. C **80**, 064323 (2009).

[67] A. Arima, K. Shimizu, W. Bentz, and H. Hyuga, Adv. Nucl. Phys. **18**, 1 (1986); A. Arima and H. Hyuga, in *Mesons in Nuclei*, edited by D. H. Wilkinson and M. Rho (North-Holland, Amsterdam, 1979), Vol. II, p. 683.

[68] I. S. Towner, Phys. Rep. **155**, 263 (1987); I. S. Towner and F. C. Khanna, Nucl. Phys. A **399**, 334 (1983).

[69] N. J. Stone, At. Data Nucl. Data Tables **90**, 75 (2005).

[70] N. J. Stone, Technical Report No. INDC(NDS)-0794, 2019 (to be published).

[71] A. I. Morales, G. Benzoni, A. Gottardo, J. J. Valiente-Dobón, N. Blasi, A. Bracco, F. Camera, F. C. L. Crespi, A. Corsi, S. Leoni, B. Million, R. Nicolini, O. Wieland, A. Gadea, S. Lunardi, M. Górska, P. H. Regan, Zs. Podolyák, M. Pfützner, S. Pietri *et al.*, Phys. Rev. C **89**, 014324 (2014).

[72] R. Caballero-Folch, C. Domingo-Pardo, J. Agramunt, A. Algora, F. Ameil, A. Arcones, Y. Ayyad, J. Benlliure, I. N. Borzov, M. Bowry, F. Calviño, D. Cano-Ott, G. Cortés, T. Davinson, I. Dillmann, A. Estrade, A. Evdokimov, T. Faestermann, F. Farinon, D. Galaviz *et al.*, Phys. Rev. Lett. **117**, 012501 (2016).

[73] R. Caballero-Folch, C. Domingo-Pardo, J. Agramunt, A. Algora, F. Ameil, Y. Ayyad, J. Benlliure, M. Bowry, F. Calviño, D. Cano-Ott, G. Cortès, T. Davinson, I. Dillmann, A. Estrade, A. Evdokimov, T. Faestermann, F. Farinon, D. Galaviz, A. R. García, H. Geissel *et al.*, Phys. Rev. C **95**, 064322 (2017).